Stratigraphy, mineralogy and geochemistry of the Upper Laetolil tuffs including a new tuff 7 site with footprints of *Australopithecus afarensis*, Laetoli, Tanzania

Anatoly N. Zaitsev[a,b,*], Lindsay McHenry[c], Anton I. Savchenok[a], Stanislav Strekopytov[b,1], John Spratt[b], Emma Humphreys-Williams[b], Victor V. Sharygin[d], Evgeny S. Bogomolov[e], Anton R. Chakhmouradian[f], Olga A. Zaitseva[g], Andrei A. Arzamastsev[e,h], Ekaterina P. Reguir[f], Larissa Leach[i], Michael Leach[i], Joshua Mwankunda[j]

[a] *Department of Mineralogy, St. Petersburg State University, University Emb. 7/9, St. Petersburg, 199034, Russia*
[b] *Image and Analysis Centre, Department of Earth Sciences, Natural History Museum, Cromwell Road, London, SW7 5BD, UK*
[c] *Department of Geosciences, University of Wisconsin-Milwaukee, 3209 N. Maryland Ave., Milwaukee, WI, 53211, USA*
[d] *V.S. Sobolev Institute of Geology and Mineralogy, Siberian Branch of Russian Academy of Sciences, Koptuga pr. 3, Novosibirsk, 630090, Russia*
[e] *Institute of Precambrian Geology and Geochronology, Russian Academy of Sciences, Makarova nab 2., St. Petersburg, 199034, Russia*
[f] *Department of Geological Sciences, University of Manitoba, Manitoba, R3T2N2, Canada*
[g] *Manege, Central Exhibition Hall, 1 Isaakiyevskaya Square, St. Petersburg, 190000, Russia*
[h] *Department of Petrography, St. Petersburg State University, University Emb. 7/9, St. Petersburg, 199034, Russia*
[i] *GMP Consulting Engineers Ltd., 19 Haile Selassie Road, P.O. Box 425, Arusha, Tanzania*
[j] *Ngorongoro Conservation Area Authority, P.O. Box 1, Ngorongoro Crater, Arusha, Tanzania*

ARTICLE INFO

ABSTRACT

The Upper Laetolil marker Tuffs 1 to 8 are mineralogically similar rocks, but heterogeneous in terms of their texture, structure, proportion of primary minerals, volume of cement and degree of low-temperature alteration. Originally they were deposited as crystal and/or vitric ash of evolved melilite-nephelinitic composition and not as melilitite-(natro)carbonatite. Occurrence of carbonate-silicate melt inclusions in primary minerals supports R. Hay's conclusion that the ash could have erupted from a carbonatitic volcanic source. Primary minerals (melilite, clinopyroxene, garnet, perovskite, magnetite) in the tuffs are characterised by wide variations in their compositions and two and even more mineral populations are present within each marker tuff. Thus, any correlation between the tuffs from different localities on the basis of mineral composition is very difficult to impossible. Tuff 7, with footprints of *Australopithecus afarensis,* is a very heterogeneous unit both vertically and laterally that formed during four major eruption events. Trace-element geochemistry and Sr–Nd isotopic data for Tuffs 6, 7 and 8 suggest that compositionally different volcanic sources were involved in their formation. Initial $^{87}Sr/^{86}Sr$ and $^{144}Nd/^{143}Nd$ ratios also show that the Sadiman volcano should not be considered as a source for these three marker tuffs at Laetoli. Only Essimingor and Mosonik volcanoes produced rocks that are mineralogically and geochemically similar to the Upper Laetolil marker tuffs, though these volcanoes lie about 100 km from Laetoli.

1. Introduction

The Laetoli palaeoanthropological site is located on the SW flank of the Ngorongoro Volcanic Highlands in northern Tanzania (Fig. 1). It has been studied intensively over the last 75 years owing to several important palaeoanthropological findings associated with various Laetoli tuffs; for further details, see Harrison, 2011, Harrison, 2011 and references therein. Laetolil tuffs are exposed within an area of about 1600 km^2, with three main areas of outcrop: Laetoli, Kakesio and Esere-Noiti. Within the Laetoli area, the tuff-bearing stratigraphy is subdivided into several Beds with a total thickness of about 152 m (Hay, 1987; Harrison, 2011). These units are (from oldest to youngest): 1) Lower Laetolil Beds; 2) Upper Laetolil Beds; 3) Lower Ndolanya Beds; 4) Upper Ndolanya Beds; 5) Naibadad Beds; 6) Olpiro Beds; 7) Lower

---

Fig. 1. Major volcanoes in the Crater Highlands and the Gregory rift - shaded and coloured SRTM elevation model (February 2000). Africa image: coloured SRTM elevation model (February 2000). Courtesy NASA/JPL/NIMA.

Ngaloba Beds; and 8) Upper Ngaloba Beds.

The Upper Laetolil (UL) tuffs (Fig. 2) are particularly well known because of their association with hominin remains and non-hominin fossils (Harrison, 2011, Harrison, 2011). Laetoli is also unique in its preservation of footprint trails assumed to have been left by *Australopithecus afarensis* in the so-called Footprint tuff located at Locality 8, Site G and Site S; the prints of numerous animals are also known within this tuff (Leakey and Hay, 1979; Musiba et al., 2008; Masao et al., 2016).

The Laetolil tuffs, and especially the upper units, are better studied compared to other tuffs from this area. Their general geology, stratigraphy, geochronology, petrography and mineralogy have been described by Hay (1978, 1987), Hay and O'Neil (1983), Drake and Curtis (1987), Barker and Milliken (2008), McHenry (2011), Deino (2011), Ditchfield and Harrison (2011), Zaitsev et al. (2011, 2015) and Kasanzu et al. (2016).

Recent $^{40}Ar/^{39}Ar$ ages based on sanidine, anorthoclase, biotite and hornblende from different Laetoli tuffs (Deino, 2011) have provided precise information on Laetoli chronostratigraphy: the Lower and Upper Laetolil Beds are 4.36–3.85 and 3.85–3.63 Ma old, respectively, the Lower and Upper Ndolanya Beds are 3.58 and 2.66 Ma, respectively, the Naibadad Beds are 2.16–2.06 Ma, and the Olpiro Beds are < 2.06 Ma in age. The interpolated age of the Footprint tuff is 3.66 Ma.

The nearby Sadiman volcano has long been considered the source for the Laetolil Beds, based in large part on its proximity (directly adjacent) and its age (4.5–3.7 Ma: Curtis and Hay, 1972; Bagdasaryan et al., 1973; 4.63–4.02 Ma: Mollel et al., 2011), though recent detailed mineralogical and geochemical analysis (Zaitsev et al., 2011, 2015)
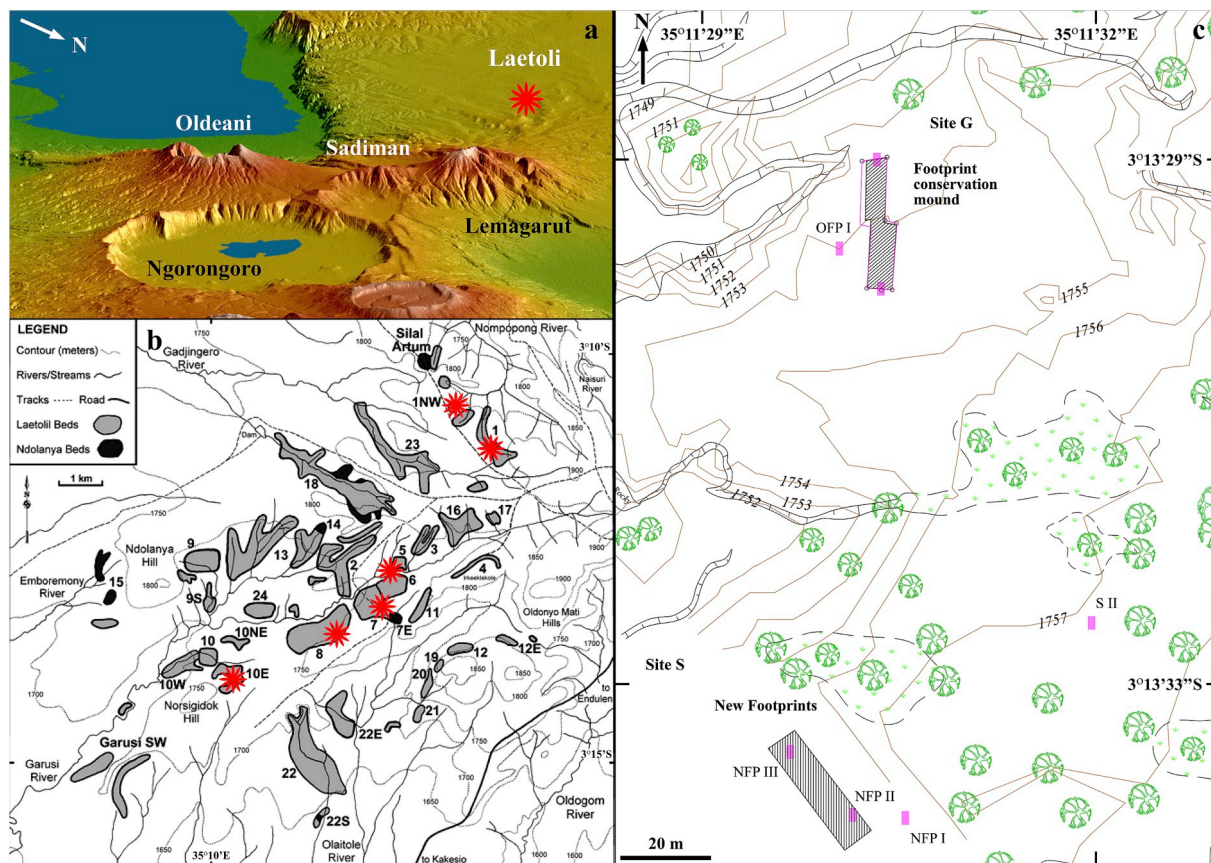

Fig. 2. Laetoli localities and site maps: (a) major volcanoes in the southern Crater Highlands area, shaded and coloured SRTM data (February 2000), orientation: view 35° south of west, 15° below horizontal, courtesy NASA/JPL/NGA; (b) main outcrops of the Upper Laetolil and Upper Ndolanya tuffs (red stars show studied localities, Ditchfield, Harrison, 2011); (c) topographic map of sites G and S of Locality 8 showing studied pits (pink rectangles, GMP Consulting Engineers Ltd, 2014). (For interpretation of the references to colour in this figure legend, the reader is referred to the Web version of this article.)
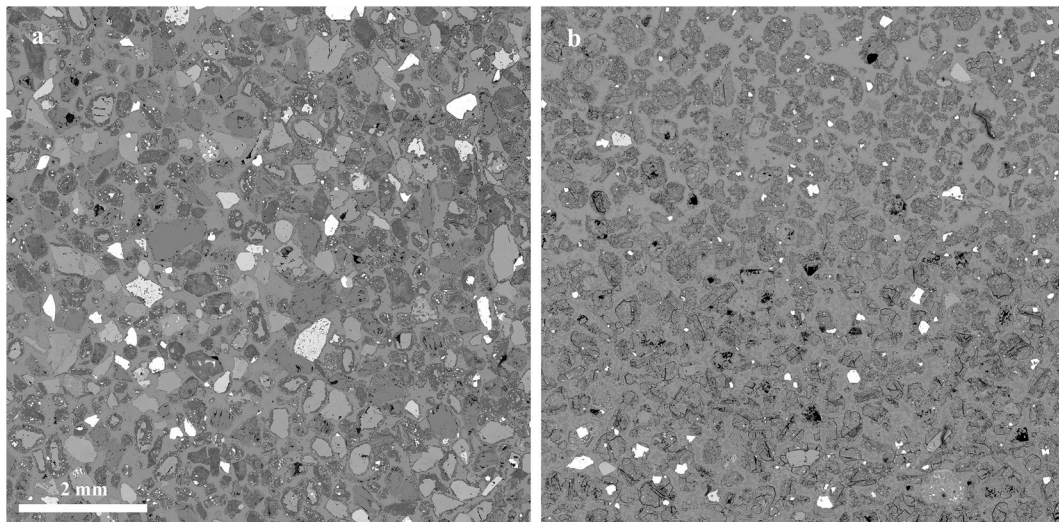
Fig. 3. Back-scattered electron (BSE) images. (a) The crystal-rich Tuff 4 and (b) the crystal-poor Tuff 3. Dark gray: montmorillonite, gray: calcite, light gray to white: clinopyroxene, garnet, perovskite and magnetite.

suggests some fundamental differences that need to be addressed. Alternative regional sources that also produced nephelinites of potentially appropriate composition, and which could be old enough to have been the source of the Laetolil tephra, include the Mosonik and Essimingor volcanoes, which both lie about 100 km from Laetoli (to the north and east, respectively). Early K/Ar dates for Essimingor (Evans et al., 1971) ranged from 4.89 to 3.20 Ma, though more recent ^{40}Ar/^{39}Ar dates are much older, 5.76–5.91 Ma (Mana et al., 2012). Radiometric dates for Mosonik range from 4.01 to 3.08 Ma (Isaac and Curtis, 1974; Manega, 1993; Muirhead et al., 2016), and they are comparable with the ages of the Lower and Upper Laetolil tuffs. Oldoinyo Lengai, Kerimasi and Embagai also produced nephelinites, but are much too young to be reasonable sources for the Laetolil Beds (Dawson, 2008).

Compositional data for major primary minerals from the Lower and the Upper Laetolil tuffs were published by McHenry (2011) and compositions of perovskite and magnetite were used for discrimination of the UL tuffs. Upper Laetolil Tuff 7 was studied in more detail because it preserves *Australopithecus afarensis* footprints within it. A general description of Tuff 7 was given by Hay (1978, 1987); its texture, structure and calcite composition were described by Barker and Milliken (2008), and more of recent studies on tuff mineralogy were published by McHenry (2011) and Zaitsev et al. (2011, 2015).

In this study, we extend available data for the Upper Laetolil tuffs with particular attention to stratigraphy, mineralogy and geochemistry (including radiogenic isotopes) of Sites G and S at Locality 8, which contain recently discovered new footprints of *Australopithecus afarensis* (Fig. 2). The purpose of the study was to acquire various data that can be useful for tuff correlation between different localities and particularly for discrimination of individual tuff layers within Tuff 7. Also, new mineralogical and geochemical data for the Laetolil tuffs have been compared with those from the nearby Sadiman volcano, which is still considered by some to be the source of the Laetolil tuffs (Kasanzu et al., 2016), and with two other volcanoes in the region (Essimingor and Mosonik) that are compositionally similar.

2. Upper Laetolil tuffs

Within the Upper Laetolil tuffs, three principal tuff varieties (lithofacies) were described by Hay (1987), i.e. aeolian tuff (75 vol%), water-worked tuff (5 vol%) and air-fall tuff (20 vol%). Some of the aeolian tuffs, particularly those with plutonic xenoliths, could in fact be lahar deposits (Ditchfield and Harrison, 2011). Water-worked tuffs are interpreted as fluvial (common) and pond (rare) deposits (Ditchfield and Harrison, 2011).

Air-fall tuffs are primary ash-fall deposits that were divided into two groups by Hay (1978, 1987): (1) medium-to coarse-grained tuffs represented by 34 layers (typically 1–15 cm, but locally up to 60 cm thick), including eight marker tuffs referred to as Tuff 1 through Tuff 8 (oldest to youngest) and occurring throughout the Laetoli area, and (2) discontinuous fine-grained tuffs (consisting of 25 layers, 1–2 cm, and rarely up to 5 cm thick).

The marker tuffs form prominent, often resistant layers within the Upper Laetolil Beds, ranging from 1 to 10 cm (Tuff 1) to 1.2 m (Tuff 5) in thickness. Some tuffs form ledges with a cm-to decimeter-scale polygonal weathering pattern on the top surface (e.g., Tuff 6). They contain reworked layers and the upper tuff layer is sometimes enriched in coarser (up to 2 cm) rock fragments (e.g., Tuff 3). The air-fall tuff units can be fine-to medium- or even coarse-grained, and some exhibit grading. Thin clay layers between volcaniclastic layers within some tuffs indicate hiatuses during ash deposition.

The tuffs comprise crystals of various size (up to 3 mm) and "globules" (described as spherical or near-spherical particles by Hay, 1978) or "pellets" (pyroclastic particles that are rounded, but smaller than lapilli in the terminology of Barker and Milliken, 2008), resulting in a pisolitic texture for some tuffs. The term "pellet" is adopted also in the present study. Volumetric proportion between crystals and pellets varies between different tuff layers from crystal-rich/pellet-poor to crystal-poor/pellet-rich varieties (Fig. 3).

Two mineral assemblages are distinguished in the samples of Tuffs 1 to 8 (Table 1). The first assemblage includes relicts of primary minerals (in total, 21 species were identified), with clinopyroxene, garnet, magnetite and perovskite occurring in all studied samples of the marker tuffs. Nepheline, apatite, phlogopite, titanite and sanidine are less common and melilite is observed in Tuff 7 only.

Primary minerals occur as euhedral, subhedral and anhedral grains (crystals and their fragments) and are covered by a thin layer consisting of montmorillonite and magnetite (former volcanic glass). Many of these crystals show corrosion and are replaced by montmorillonite, calcite and/or phillipsite. Some pellets contain intergrowths of crystals representing up to four different minerals, with magnetite + perovskite being the most typical association, and clinopyroxene + garnet + magnetite + perovskite as the most complex assemblage.

This primary paragenesis is intimately associated with authigenic minerals that formed during ash (tuff) alteration and cementation, including calcite, montmorillonite and phillipsite, with much less

Table 1
Mineralogy of the Upper Laetolil marker tuffs.

Tuff	Tuff 1	Tuff 2	Tuff 3	Tuff 4	Tuff 5	Tuff 6	Tuff 7	Tuff 8
Primary minerals								
Clinopyroxene (cpx)	+ + +	+ + +	+ + +	+ + +	+ + +	+ + +	+/+ + +	+ + +
Garnet (grt)	+ + +	+	+	+ + +	+ + +	+ + +	+/+ + +	+ + +
Magnetite (mag)	+ + +	+ + +	+ + +	+ + +	+ + +	+ + +	+/+ + +	+ + +
Perovskite (prv)	+ + +	+ + +	+ + +	+ + +	+/+ + +	+ + +	+/+ + +	+ + +
Nepheline (nph)				+ + +	+/+ + +	+	/+ + +	
Melilite (mll)							/+	
Apatite	+ +		+	+ + +	+	+ +	+/+ + +	+ +
Phlogopite (phl)	+		+	+	+	+ +	/+ + +	+/+ +
Titanite (ttn)				+	+		/+	+ +
Sanidine			+			+	/+	+
Kaersutite							/+	
Wollastonite						+		
Ilmenite							/+	
Pyrrhotite				+		+	/+	
Chalcopyrite							/+	+
Nb-rutile								+
Calcite (cal)	+		+		+	+	+/+ +	+
Secondary minerals								
Calcite (cal)	+ + +	+ + +	+ + +	+ + +	+ + +	+ + +	+ + +	+ + +
Montmorillonite (mnt)	+ + +	+ + +	+ + +	+ + +	+ + +	+ + +	+ + +	+ + +
Philipsite (php)	+ + +		+ + +	+	+ + +	+	+/+ + +	+/+ + +
Baryte							+	+
Celestine								+
Analcime							+	
Dolomite	+							
Ba–Mn hydroxide						+	+	
Pseudomorphs 1	+ + +	+ + +	+ + +	+ + +	+ + +	+ + +	+ +/+ + +	
Pseudomorphs 2	+	+	+	+	+	+	+/+ +	

Tuff 7 is a heterogeneous rock with large variations in mineral content between different layers. Clinopyroxene: diopside, hedenbergite and aegirine-augite; garnet: andradite and schorlomite; melilite: åkermanite and alumoåkermanite. Pseudomorphs 1 – tabular and prismatic-shaped pseudomorphs after melilite; pseudomorphs 2 - square- and stubby prismatic-shaped pseudomorphs after nepheline. + + + - common, + + - minor, + - rare, empty field – mineral was not observed.

common baryte, celestine and Ba–Mn hydroxide(s). No fresh, unaltered glass was found in pellets in any of the studied samples. A high degree of tuff alteration was previously reported by Hay (1978, 1987). The marker tuffs contain pellets with tabular, prismatic- and square-shaped aggregates consisting of polycrystalline montmorillonite grains, and considered to be pseudomorphs after a silicate mineral, possibly melilite (see Fig. 7 in Hay, 1978). The proportion of such pellets varies among different tuffs; they are observed in all samples from Tuffs 1 to 7, but none were found in Tuff 8. Less common are square- and stubby prismatic-shaped pseudomorphs, which probably resulted from nepheline alteration.

The marker tuffs also contain rare accessory minerals that can be considered xenocrystic and possibly derived from a granitic or metamorphic source rocks; e.g., Tuff 7 contains oligoclase $(Na_{0.84}Ca_{0.14}K_{0.02})(Al_{1.14}Si_{2.86}O_8)$ and even quartz.

3. Tuff 7

Field observations at outcrops at Localities 1 and 7, and in four pits (OFP I, NFP I, NFP II and S II) within the area of sites G and S at Locality 8 (Fig. 2), as well as published data (Hay, 1978, 1987; Barker and Milliken, 2008; McHenry, 2011, Zaitsev at al., 2011, 2015) show that Tuff 7 is very heterogeneous. Different localities and even different pits within the same locality show different stratigraphy in terms of the observed rock types and their thickness (Fig. 4, Table 2).

Our data confirm the interpretation of Hay (1987) that Tuff 7 consists of two major parts: (I) the upper Augite-biotite tuff and (II) the lower Footprint tuff. The latter was subdivided into two units (upper and lower) by Hay (1978) and into three units in this study: (1) laminated tuff, (2) white (to light gray) tuff, and (3) gray to dark gray tuff. Laminated tuff corresponds to the upper unit of Hay (1978), whereas the white and gray tuffs are both parts of his lower unit (Fig. 5). The

surface of the white tuff is a Horizon B with abundant animal and *Australopithecus afarensis* footprints.

Thin calcite layers were observed at Localities 1 and 7. At Locality 1, calcite forms a discontinuous layer (up to 9 mm thick) between the upper aeolian and Augite-biotite tuffs, whereas at Locality 7, a discontinuous calcite layer (up to 3 mm thick) occurs between the laminated and white tuffs.

The Augite-biotite tuff is a white-gray medium-to coarse-grained well-cemented crystal tuff (Fig. 6a). Its thickness varies from 18.0 cm to 23.5 cm at Sites S and G (S II and OFP I pits at Locality 8) and reaches 28.0 cm at site A at Locality 7. The Augite-biotite tuff consists of crystals (50–78 vol%) ranging between 200 μm and 2 mm in size and pellets with a diameter between 250 and 750 μm. The tuff is slightly stratified, with at least four layers, which show differences in colour, mineral content and grain size. It is a very thinly to thinly bedded rock. It has the highest density (2.27–2.69 g/cm^3) and lowest porosity (7.63–7.92 vol%) of all the tuff layers within the Footprint tuff.

The crystals are anhedral to euhedral in shape and their size increases upward (inverse graded bedding). Nearly all crystals are rimmed by a thin (10–200 μm) opaque to translucent layer of black to brown material. The layer is interpreted as altered glass coating on mineral grains. Primary minerals include clinopyroxene, phlogopite, nepheline, magnetite, perovskite, garnet and apatite (Fig. 6a). Nepheline appears to be the least stable mineral and is commonly replaced by montmorillonite and calcite (Fig. 6b and c).

The pellets are translucent to transparent in transmitted light with a distinct yellow-brown to orange colour. They consist of a mixture of isotropic and anisotropic material. X-ray diffraction (XRD) and energy-dispersive spectrometry (EDS) show that montmorillonite is the major mineral within the pellets (up to 90 vol%). Phillipsite is also present in appreciable amounts in some pellets, reaching 50 vol%. Fine-grained magnetite is another common constituent of the pellets, and is typically
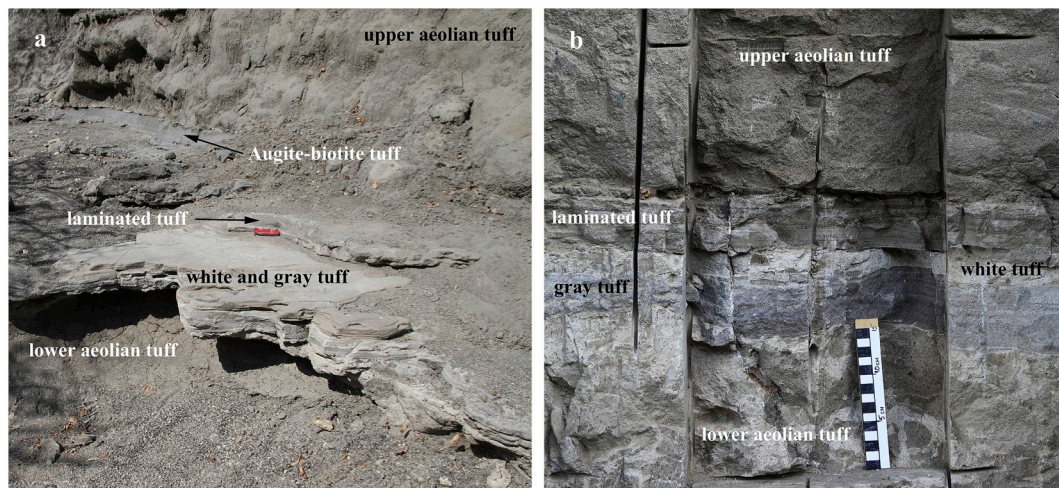
Fig. 4. Vertical sections of Tuff 7 (a) at Locality 1 and (b) at the NFP II pit, site S, Locality 8. Red knife is 11 cm and black-white scale is 15 cm. (For interpretation of the references to colour in this figure legend, the reader is referred to the Web version of this article.)

confined to their rims. The pellets are highly heterogeneous in terms of their shape, internal structure and composition (Fig. 6c and d). There are several varieties of the pellets, including those devoid of any crystals, pellets with an insignificant proportion of crystals, and those with or without distinct "euhedral to subhedral" tabular pseudomorphs. Although no relics of primary mineral(s) were found in the pseudomorphs, they appear to have formed after a melilite-group mineral.

The crystals and pellets are well cemented by calcite and montmorillonite (Fig. 6). Two varieties of calcite cement are distinguished on the basis of colour, grain size, and mineral assemblage. The first, dominant variety of cement consists of polycrystalline colourless anhedral to subhedral calcite grains (50–250 μm). The second variety consists of a mixture of calcite (up to 50 μm in size), phillipsite (as monomineralic segregations or intergrowths with calcite) and montmorillonite (filling pockets and veinlets). Other secondary minerals include a Ba–Mn hydroxide (hollandite?) and, less commonly, baryte and/or celestine.

The laminated unit is gray, fine-to medium-grained vitric tuff, which has been completely devitrified and altered (Fig. 7a and b). Its thickness varies from 4 cm (in pit NFP I) to 8 cm in pit OFP I at Locality 8. It has a clear and sharp contact with the Augite-biotite tuff and is characterised by significant changes in texture and mineralogy with respect to the latter. The tuff consists of pellets (75–80 vol%, 50–300 μm in diameter) with a small proportion of crystals typically

measuring up to 75 μm and rarely up to 150 μm in size (Fig. 7a and b). No significant difference in pellet or crystal size was observed for the bottom, middle and top layers of the tuff. Only the topmost, 4-mm thick layer at the contact with the Augite-biotite tuff is coarser, with pellets and crystals ranging in size between 400 and 900 μm. The unit as a whole is well stratified (with layer thickness ranging between 1 mm and 1 cm) and can be classified as thinly to thickly laminated tuff. Macroscopically, the laminated tuff has a clayey appearance, low density (1.80–1.94 g/cm³) and disintegrates quickly in contact with water.

Rare crystals within the pellets are represented by euhedral to subhedral magnetite, with few crystals of clinopyroxene, apatite, garnet and extremely rare perovskite in the top layer at the contact with the Augite-biotite tuff. The tuff also contains few anhedral to euhedral single crystals of calcite up to 300 μm in size which, in some cases, enclose relics of nepheline, forming partial pseudomorphs after this mineral (Fig. 7b–c). Most of these calcite grains show twinning, which was not observed in the calcite cement.

The morphology and internal structure of the pellets are similar to those in pellets of the Augite-biotite tuff. Montmorillonite is the principal constituent of the pellets, whereas fine-grained magnetite (< 25 μm in diameter, rarely up to 75 μm) occurs as a minor phase. The pellets are highly heterogeneous and often contain euhedral tabular, prismatic and square-shaped pseudomorphs (Fig. 7d). The latter are interpreted to result from complete replacement of nepheline. No fresh

Table 2
General stratigraphy of Tuff 7 (listed from the youngest to the oldest units).

Locality	Locality 8				Locality 7		Locality 1
Site	S	S	S	G	Site A	Site A	
Reference	this study	this study	this study	this study	this study	Hay (1987)	this study
Pits	NFP I	NFP II	S II	OFP I	outcrop	outcrop	outcrop
Altitude/elevation, m	1755	1755	1757	1754			
Pit depth, cm	85	110	164	133			
Soil, cm	30–39	28–30	39–40	9–12			
Upper aeolian tuff, cm	37–46	34–36	90–91	absent	not measured	not measured	not measured
Augite-biotite tuff, cm	absent	absent	18	22–23.5	27–28	15–50	25
Laminated tuff, cm	4–6	6	5	5–8	3–4	4–6	5–6
White tuff with footprints, cm	3–3.5	3–3.5	3–3.5	1	0.5–1	} 7-10	1–2
Gray tuff, cm	> 2.5	6–7	7.5–8	3-5[a]/5–6[b]	8–9		3–4
Lower aeolian tuff, cm	not excavated	> 30	> 1	> 73	not measured	not measured	not measured

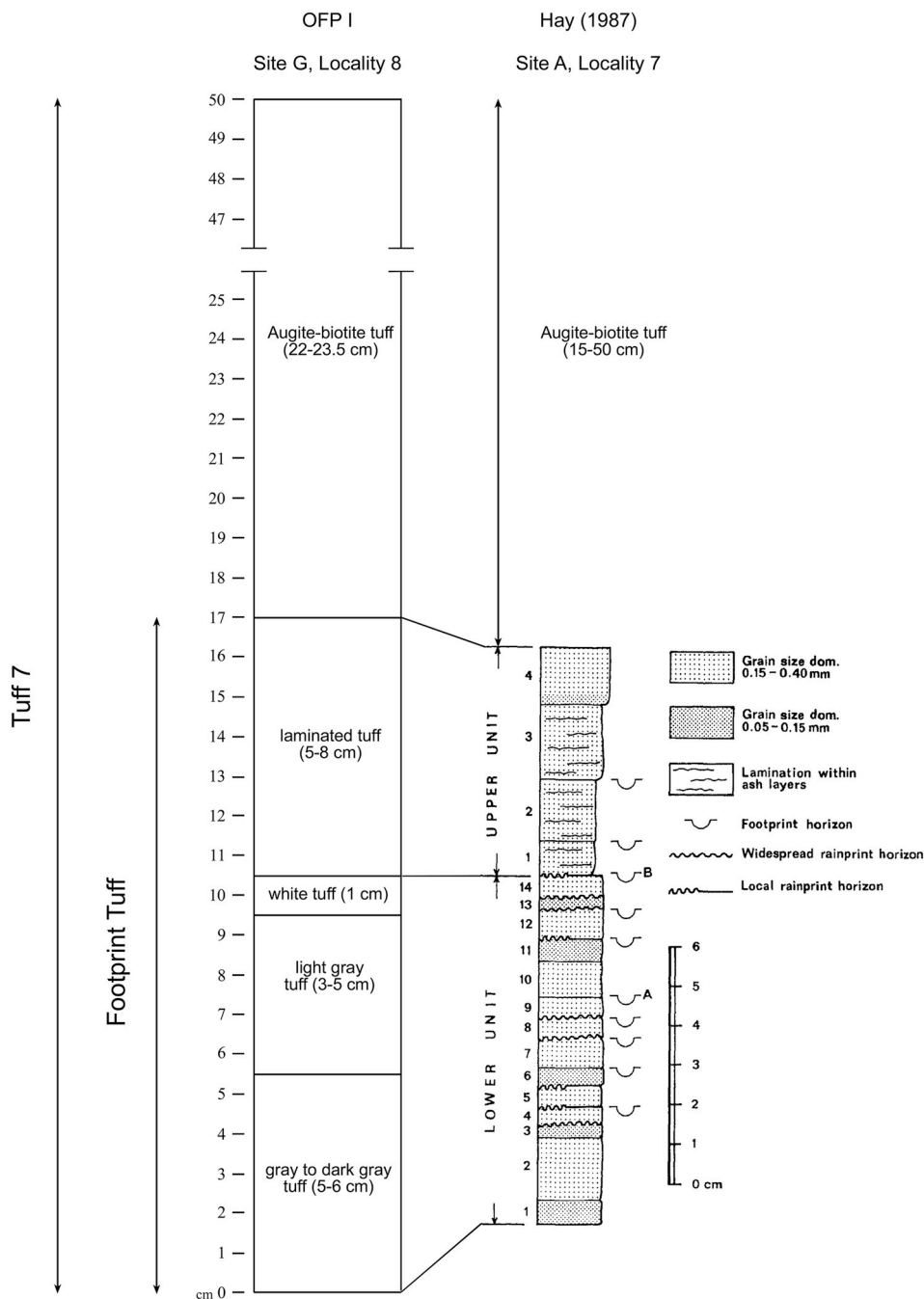[a] - light gray tuff.

[b] - dark gray tuff.

Fig. 5. Comparison of the vertical sections at site G (Locality 8) – OFP I and at site A (Locality 7) (Fig. 2.6 in Hay (1987)).

unaltered glass was detected in any of the pellets.

Montmorillonite and calcite are the principal components of the cement. Two different varieties of the cement are present. In the first variety, both minerals form fine-grained intergrowths with grain sizes up to 25 µm, resembling spotted aggregates (Fig. 7b–d). The second variety of cement is represented by monomineralic sparry calcite forming amoeboid aggregates (Fig. 7a). Phillipsite is also found in the cement near the contact with the Augite-biotite tuff, whereas other secondary minerals including Mn(± Ba) hydroxides are also present.

BSE images show that the laminated tuff is a highly porous rock with dominant porosity in the form of circum-granular pores around the pellets (Fig. 7). This could be a result of deformation during the preparation of thin sections. However, back-scattered-electron (BSE) and secondary-electron (SE) images of the surface of gently broken samples confirm abundant primary circum-granular, intergranular and intragranular porosity.

The white tuff with the hominin and animal footprints (Horizon B) is white medium-to coarse-grained vitric tuff. It is a well-cemented, massive and homogeneous rock. The tuff thickness varies from 3 cm in pits NFP I, NFP II and S II to 1 cm in pit OFP I (Locality 8). It has a clear and sharp contact with the laminated tuff and is characterised by changes in mineralogy (particularly, by the presence of abundant calcite in the cement) and texture (Fig. 1S).

The tuff is heterogeneous in terms of the size of pellets and crystals (fine to coarse) and their distribution. It consists predominantly of pellets (about 50–60 vol%), which are not well sorted and typically range from 50 to 400 µm in diameter, rarely smaller or larger (< 500 µm), with a smaller proportion of primary minerals (< 10 vol %) of variable size. Compared to the Augite-biotite and laminated tuffs, the white tuff is characterised by a high volume of cement (about
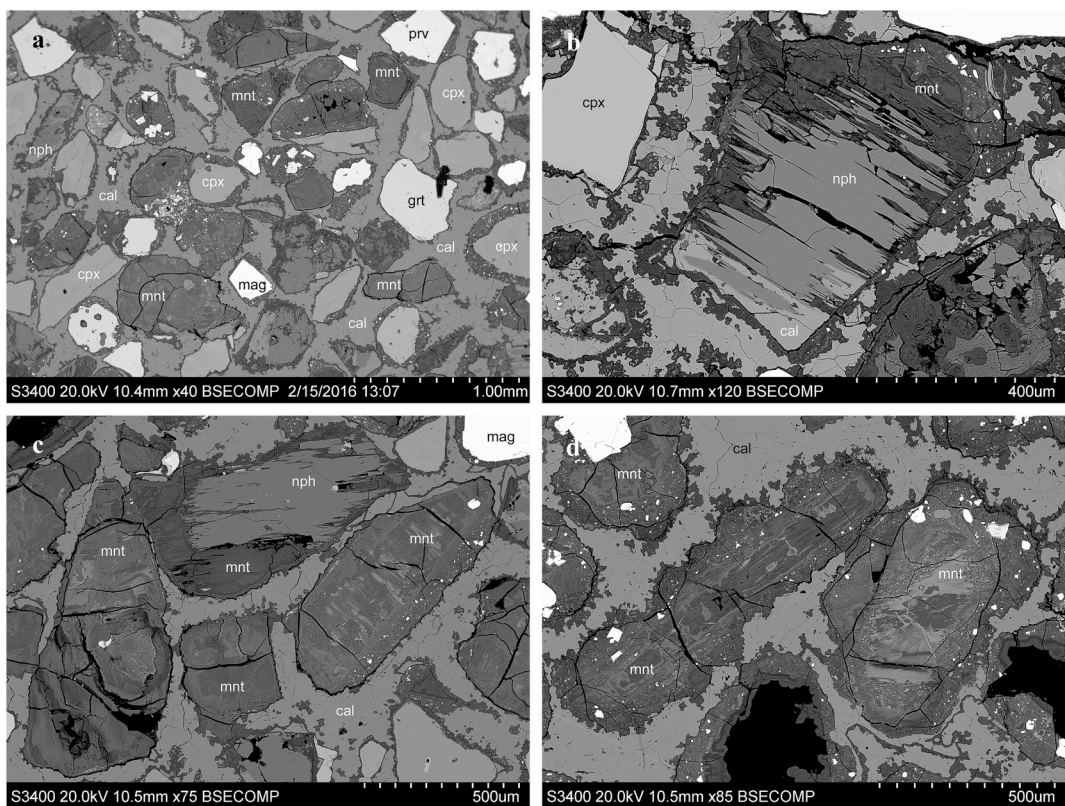
Fig. 6. (a) General view of the Augite-biotite tuff within Tuff 7, (b–c) nepheline replaced by montmorillonite and calcite, (c–d) heterogeneous pellets without and with tabular pseudomorphs. BSE images. For mineral symbols see Table 1.
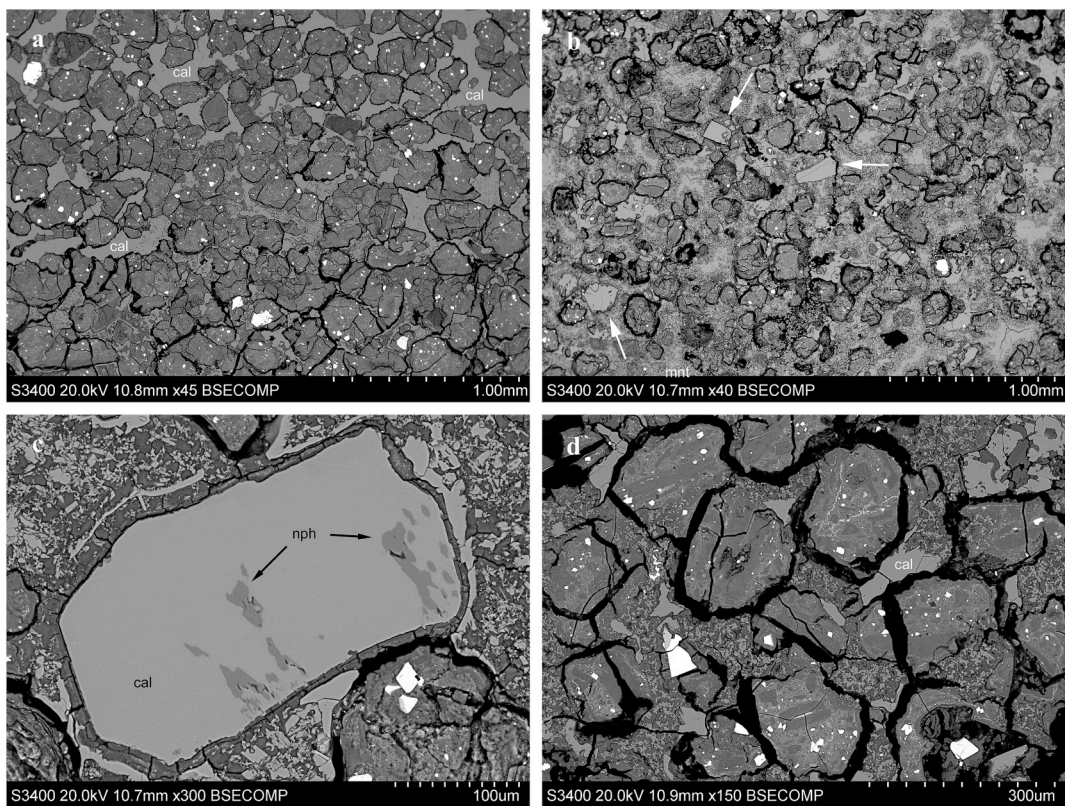

Fig. 7. BSE images. (a–b) General view of the laminated tuff within Tuff 7, (b) subhedral to euhedral calcite crystals within the tuff (white arrows), (c) calcite with relicts of nepheline, (d) pellets with tabular, prismatic pseudomorphs. White crystals: magnetite. For mineral symbols see Table 1.
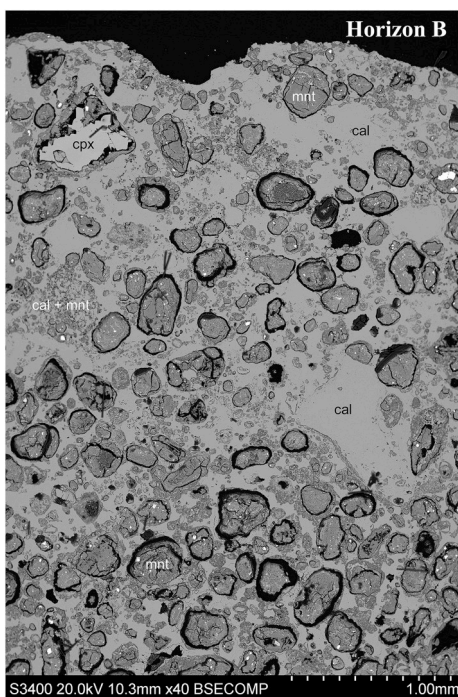
Fig. 8. Vertical section of the upper part of the white tuff with footprints within Tuff 7. White crystals: magnetite. BSE image. For mineral symbols see Table 1.

25–35 vol%). Calcite also forms thin veins, veinlets and small pockets (Fig. 8).

Density measurements for samples containing both white and underlying gray tuff gave values between 1.70 and 1.98 g/cm³.

Primary minerals occurring within the pellets as euhedral to anhedral crystals up to 1.1 mm in size include magnetite (often associated with perovskite), clinopyroxene, perovskite, garnet, as well as rare phlogopite, titanite, apatite, ilmenite, and potassium feldspar (possibly sanidine) (Fig. 9). The tuff also contains euhedral to anhedral crystals of calcite, and, in some cases, nepheline is observed within calcite as corroded relicts (Fig. 9d). Another mineral, which is unstable in the white tuff, is clinopyroxene with nearly all of its crystals showing a corroded rim (Fig. 10a and b). The crystals show strong resorption (dissolution), with their surfaces covered by newly-formed montmorillonite and phillipsite.

The white and underlying gray tuffs are the only tuff layers at Laetoli observed to contain relict fragments of a melilite-group mineral (Fig. 10c and d; see also McHenry, 2011; Zaitsev et al., 2015). Melilite was also described from aeolian tuffs by Hay (1978). All other marker tuffs, as well as aeolian tuffs, contain abundant polycrystalline pseudomorphs (montmorillonite ± calcite ± phillipsite) after a mineral resembling melilite in morphology.

The pellets are highly heterogeneous and composed predominantly of montmorillonite with magnetite as a minor phase (Figs. 8 and 1S). In some cases, calcite is present in pellets as a minor to major mineral. Phillipsite crystals are rare and were observed within a small number of pellets. Some pellets contain tabular, prismatic and square-shaped pseudomorphs.

The abundant cement of the white tuff can be subdivided into two varieties. The first, dominant variety is an aggregate consisting of montmorillonite (as aggregates up to 100 μm in size) and calcite (as subhedral crystals up to 50 and rarely 100 μm). The second variety comprises sparry calcite forming amoeboid aggregates, pockets and veinlets. Secondary Mn(± Ba)-hydroxides form dendrite-like aggregates on the surface and also occur within the tuff. The upper part of the tuff (just below the surface) contains abundant prismatic crystals of baryte, and, in addition, rare intergrowths of celestine and baryte are found in the cavities. Similar to the laminated tuff, the white tuff is a
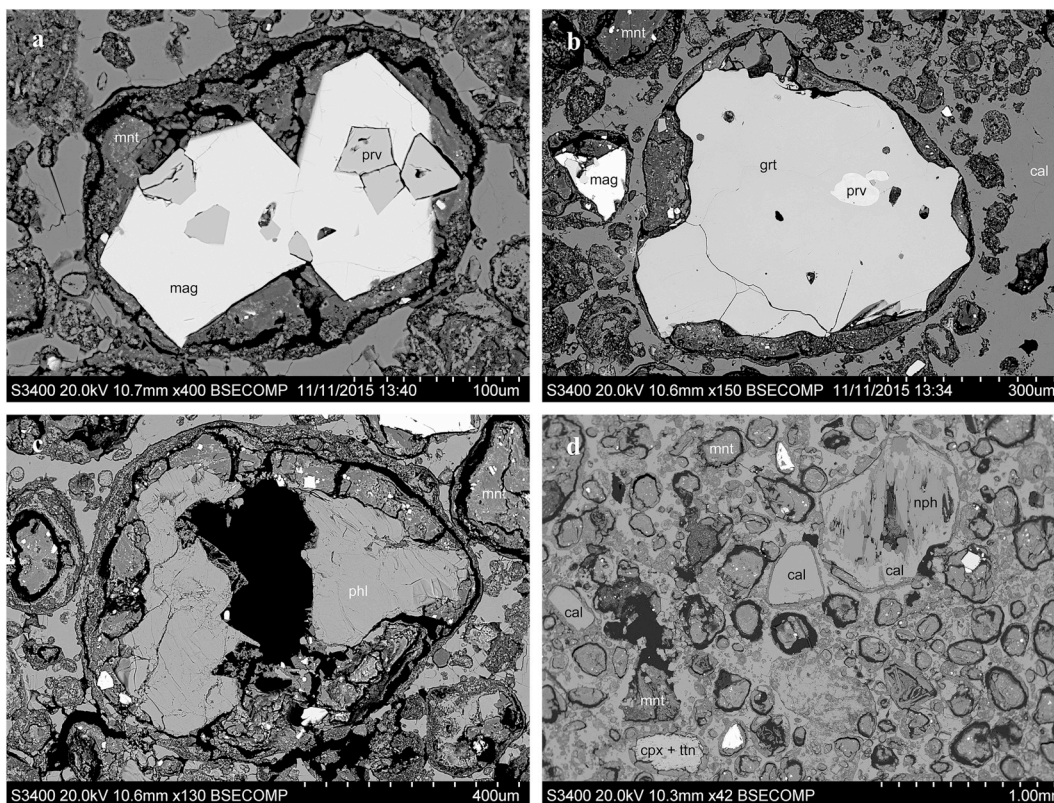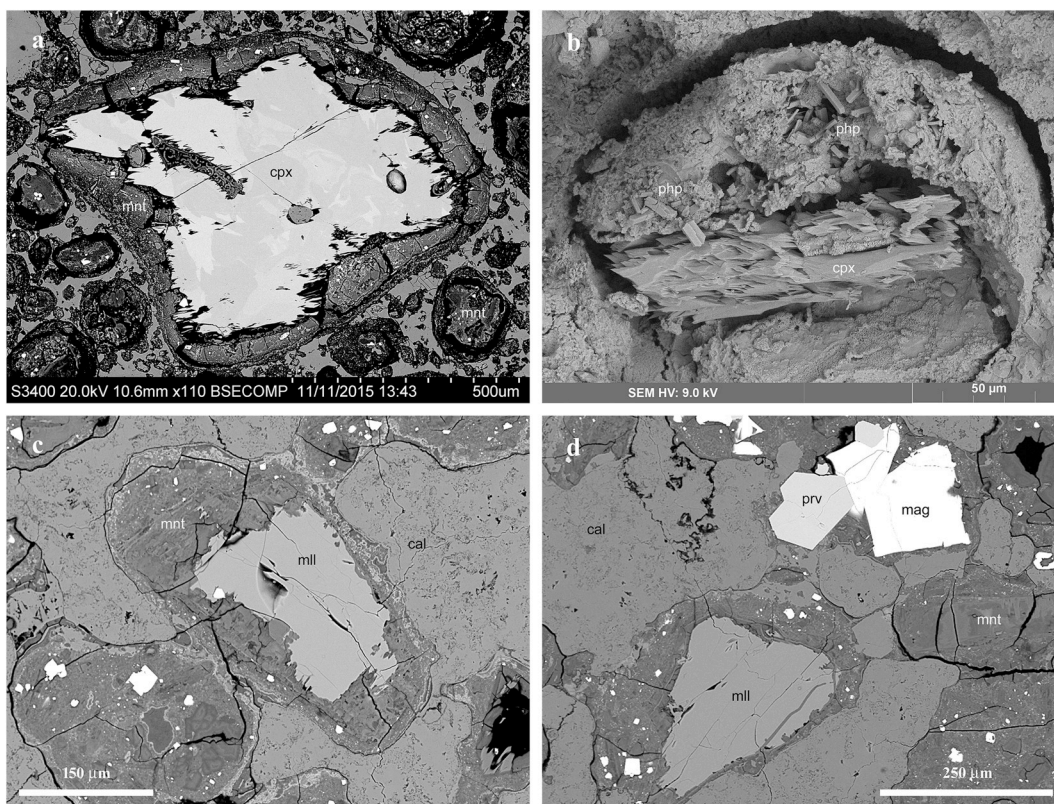

Fig. 9. Minerals of the white tuff - (a) euhedral magnetite and perovskite crystals, (b) anhedral garnet crystal with relict perovskite, (c) phlogopite crystal, (d) calcite with nepheline relicts inside the crystal and calcite without nepheline relicts. BSE images. For mineral symbols see Table 1.

Fig. 10. Minerals of the white tuff part of Tuff 7, (a) corroded and zoned clinopyroxene crystal, (b) pellet with strongly corroded clinopyroxene crystal with newly-formed prismatic phillipsite and platy montmorillonite, (c–d) corroded melilite crystals inside pellets. (a, c and d) BSE images, (b) secondary electron (SE) image. For mineral symbols see Table 1.

highly porous rock with dominant porosity in the form of circumgranular pores around the pellets. Secondary-electron microscopy (SEM) and BSE images of the surface of broken samples show all three types of pores – circumgranular, intergranular and intragranular.

X-ray microtomography gave porosity values between 25.8 and 27.8 vol%, which are significantly higher compared to the porosity calculated by Barker and Milliken (2008) from measurements on epoxy-impregnated thin sections (12.3–19.7 vol%). An estimated 97.9–98.8% of the total porosity is open porosity (i.e., interconnected pores that intersect the surface of the tuff) and the remaining 1.2–2.1% is closed porosity (isolated pores).

The gray tuff is a heterogeneous, well-cemented fine-to coarse-grained vitric tuff of light gray, gray, or dark gray colour. Its thickness ranges from 6 to 7 cm in pit NFP II to 9–10 cm in OFP I. The gray tuff has a complex contact with the overlying white tuff (Fig. 11). Only in pit OFP I, the two tuff units have a simple horizontal contact. In the other documented pits (NFP I, NFP II and S II), the contact between the

two tuffs is also clear and sharp (Fig. 12, 2S, 3S), but stratigraphic sections observed in these pits, and particularly S II, suggest a hiatus between the deposition of the gray tuff and overlying white tuff, accompanied by strong erosion of the former. This interpretation is based on the observation that the white tuff has an undulose base and contains discontinuous lenses and "inclusions" of gray tuff. In addition, the gray tuff, as well as the white tuff at S II, also contains numerous internal layers, lenses and pockets of a brown clayey material composed of calcite and montmorillonite (Figs. 11, 2S and 3S). These structures probably represent small infilled channels in the host tuff that were incised by rivulets during rainy seasons.

Like the overlying white tuff, the gray tuff comprises primarily pellets of variable size (between 30 and 600 μm) and a small proportion of crystals (5–10 vol%, 100–300 μm in size). The tuff is stratified, with the thickness of individual layers ranging between 1 mm and 2 cm, and can be termed thinly laminated to very thinly bedded tuff. Different layers are distinguished on the basis of pellet diameter, which ranges
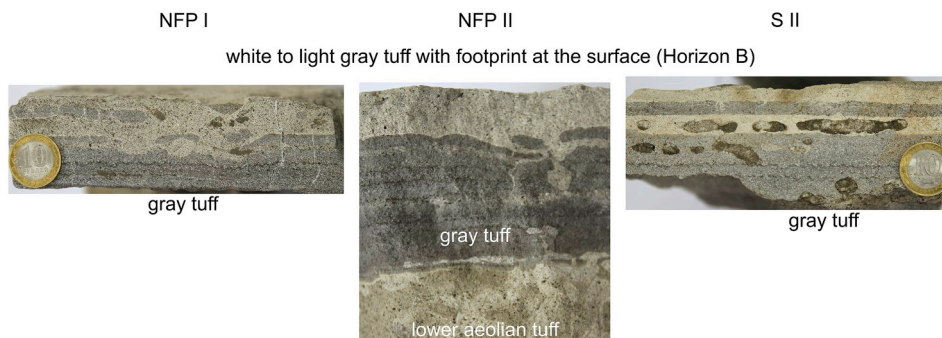
Fig. 11. Vertical section for the white and gray tuffs from different pits. Brown pockets in S II sample – calcite-montmorillonite clay. Coins are 27 mm in diameter. (For interpretation of the references to colour in this figure legend, the reader is referred to the Web version of this article.)
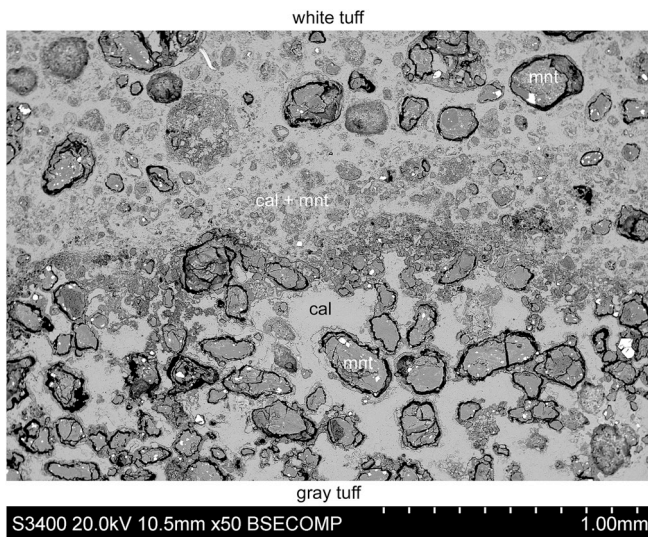
Fig. 12. Contact between the white and gray tuffs in Tuff 7. BSE image. For mineral symbols see Table 1.

from 30 to 100 μm in the lowermost layer adjacent to the lower aeolian tuff and increases upwards, reaching 400–600 μm.

The principal primary mineral is magnetite, whereas clinopyroxene, perovskite, garnet, titanite and apatite are present in much smaller proportions. They occur as anhedral to euhedral crystals. Rare subhedral to euhedral calcite crystals are found within the pellets and as discrete crystals devoid of coating (Fig. 13a).

The pellets consist of montmorillonite, magnetite and calcite, and they are similar to those in the white tuff in terms of their internal

structure. However, in comparison with the white tuff, the gray tuff is characterised by better sorting of pellets within individual layers and contains more elongate pellets with well-shaped tabular pseudomorphs (Fig. 13b).

Two varieties of cement are observed in the gray tuff; they differ in mineralogy and grain size (Figs. 12 and 13a-c). The first variety is represented by fine-grained aggregates consisting of calcite, montmorillonite and phillipsite. These minerals overgrow the pellets and form spherical aggregates, and, in addition, fill the space between pellets and central parts of relatively large primary pores often containing subhedral calcite without montmorillonite and/or phillipsite. The second type of cement is a fine-to medium-grained calcite with a low content of montmorillonite and very rare phillipsite. Sparry calcite occurs in the central part of large pores. Euhedral prismatic phillipsite crystals and platy crystals of montmorillonite are common in intergranular pores (Fig. 13d).

The gray tuff is a highly porous rock with dominant porosity in the form of circum-granular pores around the pellets, as well as intragranular pores. Porosity calculated from X-ray tomography is 22.6 vol%.

Tuff 7 is over- and underlain by gray to white aeolian tuffs (Fig. 4), which are fine-to coarse-grained and heterogeneous in texture and structure. The tuffs are well cemented and compact in outcrop, particularly at the contact with the gray tuff. Below, the lower tuff becomes softer and contains a significant amount of water. After the removal of tuff samples from outcrop, the rock loses water and becomes cracked, softer, loose and brittle. The tuffs are crosscut by calcite veinlets (1–10 mm thick), and also contain calcite-rich pockets and lenses. They also contain rare fragments of plutonic rocks up to 5 mm in size. The contacts between Tuff 7 and the aeolian tuffs are clear and sharp, and the contact between the gray and lower aeolian tuff is undulose.

The aeolian tuffs consist of a mixture of crystals (50 μm-1 mm in

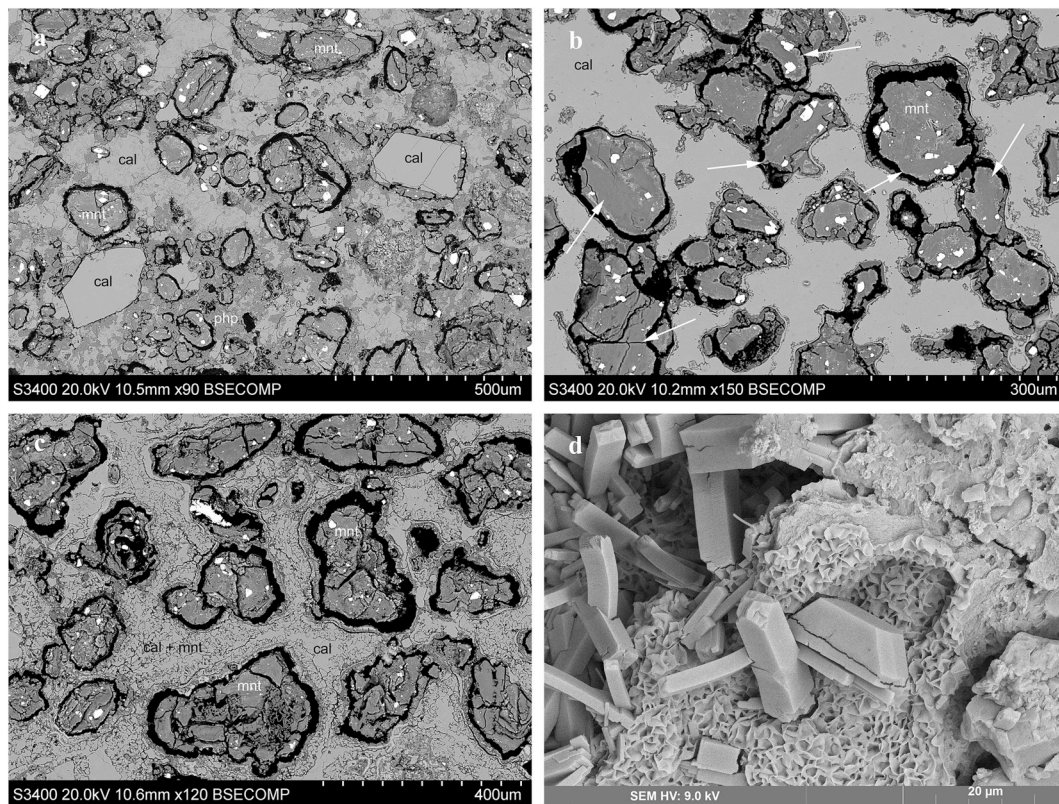**Fig. 13.** Minerals of the gray tuff in Tuff 7– (a) calcite crystals, (b) pellets with tabular, prismatic pseudomorphs (white arrows), (c) tuff cement consisting of fine-grained calcite and montmorillonite, (d) prismatic phillipsite crystals and sheets crystals of montmorillonite in intergranular pore. White crystals in (a–c) - magnetite. (a–c) BSE images and (d) SE image. For mineral symbols see Table 1.

size), pellets with and without crystals (50–100 μm to almost 1 mm in diameter), and calcite and montmorillonite in the cement. The observed minerals are clinopyroxene, magnetite, perovskite, garnet, calcite, plus rare phlogopite, titanite and kaersutite. Nepheline typically occurs as corroded relicts within calcite crystals. Isolated grains of quartz, oligoclase and microcline were observed in the upper part of the lower tuff. The majority of the minerals are present as angular (broken) fragments, but subhedral to euhedral crystals, particularly within the pellets, are also present. Plutonic rock fragments consist of fine-grained crystals of diopside, apatite, magnetite and Ti-bearing andradite; this rock is best termed apatite clinopyroxenite. Pellets of variable size and shape (spherical, elongate) consist of montmorillonite with subordinate amounts of calcite and minute crystals of magnetite. Few pellets contain tabular, prismatic-shaped montmorillonite grains, similar to those observed in Tuff 7 and were interpreted as pseudomorphs after a melilite-group mineral. The cement is a mixture of fine-grained montmorillonite, anhedral to subhedral calcite and rare phillipsite.

4. Methods

Identification of minerals in the tuffs was based on data from petrographic studies of polished thin sections and XRD measurements of selected powder samples using a Bruker D8 Focus XRD system, CuKα radiation, range 2-60° 2θ, Sol-X energy dispersive detector (for details, see McHenry, 2009). For clay mineral identification, 13 samples were analysed using a MiniFlexII (Rigaku) diffractometer, CoKα$_{1+2}$, radiation with $\lambda_{CoK\alpha1}$ = 1.78900 Å and $\lambda_{CoK\alpha2}$ = 1.79283 Å, operated at 30 kV and 15 mA. In addition, seven samples were analysed after ethylene glycol treatment and heating up to 550 °C following the procedure for clay-mineral identification (Frank-Kamenetsky, 1975, 1983; Moore and Reynold, 1997; Poppe et al., 2001). Three clay-bearing samples were also analysed by infrared (IR) spectroscopy and the IR spectra were recorded using a Bruker Vertex 70 FTIR spectrophotometer (KBr pellet, resolution 4 cm^{-1}).

Polished thin sections and slabs were studied using SEM and EDS. The samples were examined using a JEOL 5900LV and Hitachi S–3400N scanning electron microscopes equipped with an Oxford Instruments X-Max 20 spectrometer for EDS work (accelerating voltage 20 kV, beam current 2.5 nA). Electron microprobe analysis of minerals using wavelength-dispersive X-ray spectrometry (WDS) were obtained using a Cameca SX-100 instrument operated at 20 kV, 20 nA with a beam diameter of 5 μm for melilite, 10 μm for nepheline and sanidine, and 1 μm for the other phases. Well characterised natural minerals and synthetic compounds were used for calibration.

Individual mineral grains were mounted in epoxy resin and used to study silicate-melt inclusions. All samples were prepared using water-free Al$_2$O$_3$ and diamond powders to prevent the loss of water-soluble components or hydration of phases within the inclusions. Optical studies were carried out with an Olympus BX51 microscope in transmitted and reflected light. BSE images, elemental maps, and EDS analyses of minerals in the inclusions were obtained using a MIRA 3LMU SEM instrument (TESCAN Ltd.) equipped with an INCA Energy 450 XMax 80 microanalysis system (Oxford Instruments Ltd.). Qualitative EDS analyses were done at an accelerating voltage of 20 kV, a probe current of 1 nA, and accumulation time of 20 s. Correction for matrix effects was done using the XPP algorithm, implemented in the software of the microanalysis system (INCA 450). Metallic Co served for quantitative optimization (normalization to probe current and energy calibration of the spectrometer).

Raman spectroscopy was used to identify some of the phases in mineral inclusions. We used a LabRAM HR 800 mm (HORIBA Scientific Ltd.) spectrometer equipped with a CCD detector and coupled to an Olympus BX40 confocal microscope (× 100 objective) at the Institute of Geology and Mineralogy, Novosibirsk. A semiconductor laser emitting at 514.5 nm with a nominal power output of 50 mW was used for excitation. In each case, 10 spectra were recorded for 10 s each at a hole

diameter of 100 μm and integrated. The spectra were measured in the range from 100 to 1200 and from 3000 to 4000 cm^{-1}. The spectrometer was calibrated using the 520.7 cm^{-1} Raman line of elemental silicon.

Bulk tuff samples were analysed by inductively coupled plasma optical emission spectrometry (ICP-OES) and inductively coupled plasma mass-spectrometry (ICP-MS) for major and trace elements, and combustion analysis for C and H. Major and minor elements, as well as Sr and Ba, were determined by ICP-OES. For this, approximately 100 mg of the powder was fused with 300 mg of LiBO$_2$ in a Pt–Au crucible. The resulting flux was dissolved in 0.64 M HNO$_3$ before major-element abundances were determined in triplicate using a Thermo iCap 6500 Duo ICP-OES instrument. The instrument was calibrated using a range of certified reference materials (CRM), which were prepared in the same way. Basalts BIR-1 and JB-1 and granodiorite GSP-2 were analysed as unknowns for quality control. For trace-element measurements, finely powdered rock samples (dried at 105 °C for 2 h) were digested using the following protocol. About 50 mg of sample was weighed to 0.1 mg into a 10 ml fluoropolymer vessel and pre-treated with 1 ml NHO$_3$ + 4 ml HF overnight without heating. Then the samples were digested in an UltraWave® single reaction chamber microwave digestion system (Milestone Inc.) at 260 °C for 60 min (including 20 min of ramp-up time). After that, the samples were transferred into 60 ml fluoropolymer vessels, 1 ml HClO$_4$ was added to each, and the samples were evaporated to dryness at 150 °C. The residue was then re-dissolved in 2 ml HNO$_3$ + 0.2 ml H$_2$O$_2$ and made up to 50 ml with ultra-pure water (18 MOhm cm^{-1}). All acids used were of trace element analysis grade (SpA™, Romil Ltd.). Most of the trace elements were quantified by ICP-MS using a 7700x mass-spectrometer (Agilent Technologies, Inc.). V, Cr, Mn, Co, Ni, Cu, Ge, Mo, Cd, Hf, Ta, W, Ta and rare-earth elements (REE) were determined with 5 ml/min He in the collision-reaction cell to minimise molecular interferences; Li, Be, Sc, Zn, Y, Rb, Zr, Nb, Sn, Sb, Cs, Pb, Th and U were determined in "no gas" mode. Additionally, polyatomic interferences from REE and Ba affecting ^{74}Ge, ^{151}Eu, ^{157}Gd, ^{159}Tb, ^{178}Hf, ^{181}Ta and ^{182}W were mathematically corrected (Strekopytov and Dubinin, 1997; Ferrat et al., 2012). The concentrations in the procedural blanks were below the limits of detection for all elements. Accuracy of the method was checked by simultaneous digestion and analysis of CRM syenite SY-2; basalt BCR-2 (USGS) and limestone Jls-1 (GSJ) were also used for quality control.

The Rb–Sr and Sm–Nd isotopic compositions of the samples were analysed using a multi-collector TRITON mass-spectrometer operated in static mode. Two fractions were analysed from each sample: acid-soluble, obtained by treatment with 1 M HCl for 1 h, and an insoluble residual fraction. The contents of Rb, Sr, Sm and Nd were determined by isotope dilution using mixed ^{87}Rb-^{84}Sr and ^{149}Sm-^{150}Nd spikes. A preliminarily powdered sample was blended with weighed amounts of mixed ^{149}Sm-^{150}Nd and ^{87}Rb-^{84}Sr spike solutions. Then the prepared sample was dissolved in a mixture of nitric and hydrofluoric acids. Rb and Sr were separated for isotope analysis using cation exchange chromatography with AG50W-X8 resin. Sm and Nd were separated for isotope analysis in two stages. The first stage included the separation of all REE from the bulk of the sample using cation exchange chromatography with AG50W-X8 resin. The second stage included extraction chromatography using a liquid HDEHP on Teflon carrier as a cation exchange medium. A correction for Nd isotope fractionation was introduced using the normalization of the measured values to ^{146}Nd/^{144}Nd = 0.7219. The normalized ratios were adjusted to ^{143}Nd/^{144}Nd = 0.511860 in the La Jolla Nd isotope standard. A correction for Sr isotope fractionation was introduced using the normalization of the measured values to ^{86}Sr/^{88}Sr = 0.1194. The normalized ratios were adjusted to ^{87}Sr/^{86}Sr = 0.710250 in the SRM-987 Sr isotope standard. The errors for the determined Sm, Nd, Rb and Sr contents were 0.5%. The Sm and Nd blanks were 10 and 20 pg, respectively. The Rb and Sr blanks were 30 pg each. The analysis of the BCR-1 standard

yielded the following values (mean of ten measurements): 6.45 ppm Sm, 28.4 ppm Nd, $^{147}Sm/^{144}Nd = 0.1382 \pm 3$, and $^{143}Nd/^{144}Nd = 0.512656 \pm 8$; 45.9 ppm Rb, 329 ppm Sr, $^{87}Rb/^{86}Sr = 0.4023 \pm 9$, $^{87}Sr/^{86}Sr = 0.705013 \pm 16$.

5. Results

5.1. Mineral compositions

In total, 21 primary and 8 secondary minerals were identified in the UL marker tuffs during this study (Table 1).

Among the primary minerals occurring in the marker tuffs, melilite is of a particular significance because its presence indicates a specific range of magma compositions that could serve as a source for the Laetolil tuffs (Hay, 1978; Barker and Milliken, 2008; Zaitsev et al., 2015). The mineral was found only in Tuff 7 (white and gray tuff layers), whereas the other marker tuffs contain prismatic pseudomorphs, which are highly likely to have formed after melilite. Only Tuff 8 does not contain any obvious pseudomorphs that could represent replaced melilite and nepheline. Melilite occurs as corroded grains within pellets and reaches several hundred μm in length (Fig. 10), and was also observed as small crystals in magnetite-hosted melt inclusions.

Twenty-four spot analyses of melilite show a uniform composition with no obvious core-to-rim zonation (Table 3). The mineral contains 6.0–6.6 wt% MgO, 7.8–9.0 wt% Al_2O_3 and 4.3–4.8 wt% Na_2O, minor elements are Sr (0.2–0.3 wt% SrO), K, Mn and Ti (up to 0.1 wt% respective oxides). The FeO and Fe_2O_3 values calculated on the basis of stoichiometry are variable (1.3–3.7 and 0.1–3.3 wt%, respectively). On an Al–Mg–Fe^{2+} classification diagram (Fig. 14), most of the analysed points plot within the åkermanite field, but some compositions correspond to alumoåkermanite (Wiedenmann et al., 2009).

Nepheline relics with various degrees of replacement by montmorillonite, calcite and phillipsite are observed in Tuffs 4, 5 and 7 (Fig. 6b). This mineral was also documented in Tuff 6 as small
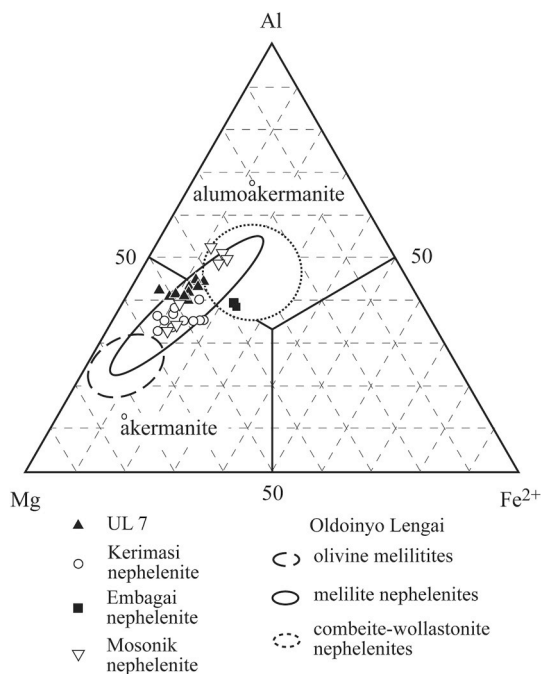

Fig. 14. Compositional variations of åkermanite and alumoåkermanite from Tuff 7. Oldoinyo Lengai data are from Wiedenmann et al. (2009, 2010), Embagai data are from Mollel (2007).

Table 3
Selected analyses of melilite from white and gray tuff layers of Tuff 7.

Sample	LA 1.09						
Analysis	1/2	1/3	1/1	1/16	1/17	1/18	1/19
SiO_2	41.96	41.98	42.33	43.35	43.52	43.37	43.24
Al_2O_3	7.89	7.86	7.90	9.03	9.03	8.47	8.54
$Fe_2O_{3calc.}$	3.25	2.26	2.57	0.06	0.99	0.46	1.00
$FeO_{calc.}$	1.28	2.27	1.92	3.72	3.02	3.50	3.09
MnO	0.10	0.10	0.11	0.05	0.09	0.09	0.07
MgO	6.30	6.30	6.47	6.09	6.09	6.11	6.30
SrO	0.24	0.26	0.19	0.22	0.20	0.17	0.18
CaO	33.18	32.76	33.20	32.58	32.75	32.87	32.66
Na_2O	4.47	4.31	4.38	4.63	4.81	4.58	4.63
K_2O	0.05	0.10	0.06	0.08	0.09	0.08	0.08
Total	98.72	98.20	99.14	99.82	100.59	99.70	99.80
Si	1.931	1.943	1.939	1.964	1.956	1.969	1.961
Al	0.069	0.057	0.061	0.036	0.044	0.031	0.039
Total	2.000	2.000	2.000	2.000	2.000	2.000	2.000
Mg	0.432	0.435	0.442	0.411	0.408	0.414	0.426
Al	0.358	0.371	0.365	0.446	0.435	0.423	0.417
Fe^{2+}	0.049	0.088	0.074	0.141	0.114	0.133	0.117
Fe^{3+}	0.113	0.079	0.089	0.002	0.034	0.016	0.034
Mn	0.004	0.004	0.004	0.002	0.003	0.003	0.003
Total	0.956	0.976	0.973	1.002	0.993	0.988	0.997
Ca	1.636	1.624	1.629	1.581	1.577	1.599	1.587
Na	0.399	0.387	0.389	0.407	0.419	0.403	0.407
K	0.003	0.006	0.004	0.005	0.005	0.005	0.005
Sr	0.006	0.007	0.005	0.006	0.005	0.004	0.005
Total	2.044	2.024	2.027	1.998	2.007	2.012	2.003

Fe_2O_3 and FeO calculated from charge balance (5 cations and 7 O).

Table 4
Selected analyses of nepheline.

Tuff	UL 4		UL 5		UL 6	UL 7	
Sample	LA 1.23		LA 1.24		LA 1.06	LA 1.09	
Analysis	1/56	1/60	1/35	1/40	1/7	1/5	1/10
SiO_2	41.49	41.20	41.78	41.24	41.88	41.68	40.92
Al_2O_3	35.31	34.68	34.92	34.90	33.53	35.19	34.66
Fe_2O_3	0.77	1.12	0.97	0.63	2.22	0.78	0.80
CaO	1.22	0.64	0.97	1.11	0.41	1.05	0.98
MgO	0.06		0.05	0.06	0.05	0.07	0.07
Na_2O	15.79	15.74	15.90	15.50	15.14	16.20	15.90
K_2O	6.12	6.74	6.33	6.53	8.17	5.90	6.39
Total	100.76	100.12	100.92	99.97	101.40	100.87	99.72
Si	3.978	3.990	4.004	3.990	4.038	3.990	3.976
Al	3.990	3.958	3.944	3.980	3.810	3.970	3.969
Fe^{3+}	0.056	0.082	0.070	0.046	0.161	0.056	0.058
Total	4.046	4.040	4.014	4.026	3.971	4.026	4.028
Na	2.935	2.955	2.954	2.908	2.830	3.007	2.995
K	0.749	0.833	0.774	0.806	1.005	0.720	0.792
Ca	0.125	0.066	0.100	0.115	0.042	0.108	0.102
Mg	0.009		0.007	0.009	0.007	0.010	0.010
Total	3.818	3.854	3.835	3.838	3.885	3.845	3.900

inclusions (up to 25 × 30 μm) within a garnet crystal (Table 1). In general, mineral compositions (88 spot analyses) from Tuffs 4, 5 and 7 are very similar with some variations for Na_2O (15.5–16.3 wt%) and K_2O (5.9–7.4 wt%) (Table 4). Minor elements are Fe (0.6–2.0 wt% Fe_2O_3) and Ca (0.2–1.7 wt% CaO). An inclusion of nepheline within a garnet crystal from Tuff 6 has a distinct composition with high K_2O (8.2 wt%) and Fe_2O_3 (2.2 wt%) and low Na_2O (15.1 wt%) contents.

On a Hamilton nepheline diagram (Hamilton, 1961) all data plot below the 500 °C isotherm (Fig. 15) and these are too low to be considered a true crystallization temperature. This could be an indication of significant changes of nepheline composition after its deposition. Sadiman nephelinites also contain nepheline with low content of the
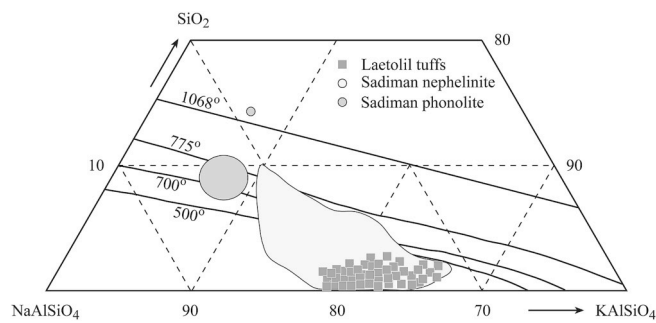
Fig. 15. Nepheline compositions (wt.%) from Tuffs 4, 5, 6 and 7. Sadiman data from Zaitsev et al. (2012), the isotherms are from Hamilton (1961).

SiO_2 end-member, but some samples contain nepheline enriched in SiO_2 and $NaAlSiO_4$ end-members and plot near the 750-700 °C isotherm (Zaitsev et al., 2012).

Clinopyroxene occurs in all marker tuffs and is always a major mineral within the primary mineral assemblage (Figs. 6a and 10a, b). Its composition has been well-studied by McHenry (2011) and Zaitsev et al. (2015) and ranges from diopside $(Ca_{0.98}Na_{0.02})$ $(Mg_{0.84}Fe^{3+}_{0.07}Fe^{2+}_{0.05}Ti_{0.03}Mn_{0.01})(Si_{1.93}Al_{0.07})O_6$ to aegirine-augite $(Ca_{0.56}Na_{0.45})(Fe^{3+}_{0.44}Fe^{2+}_{0.30}Mg_{0.21}Mn_{0.03}Ti_{0.02})(Si_{1.98}Al_{0.02})O_6$. Wide variations in mineral composition have been observed within a single tuff layer from different localities, a single sample from a tuff, and even within a singe crystal. Compositions of clinopyroxene are completely overlapping and are not suitable for correlation or discrimination of different marker tuffs.

Garnet, perovskite and magnetite are also present in all of the marker tuffs (Table 1), however, they occur in highly variable amounts, from exceptionally rare (e.g. one garnet crystal identified in Tuff 2) to major minerals (e.g. within Augite-biotite tuff of Tuff 7).

The garnet (Figs. 6a and 9b) belongs to an andradite-schorlomite solid solution and its composition (127 spot analyses) varies from Ti-poor andradite (0.8 wt% TiO_2 and 30.2 wt% $Fe_2O_{3calc.}$ in Tuff 1) to schorlomite with 18.9 wt% TiO_2 (Table 5, Fig. 16). Minor components are Na (0.1–1.6 wt% Na_2O), Mn (0.2–0.6 wt% MnO), Al (0.2–2.6 wt% Al_2O_3), Mg (< 1.6 wt% MgO) and V (0.1–0.8 wt% V_2O_3). Furthermore, Zr is also a minor element and ZrO_2 content varies from below the detection limit (bdl) low Ti andradite (TiO_2 = 0.5–6.8) up to 3.2 wt% in some schorlomite crystals with TiO_2 = 15.5–17.4 wt%. For the majority of schorlomite analyses zirconium content is, however, between 0.1 and 0.9 wt% of oxide. Garnet also contains Nb with Nb_2O_5 content between bdl and 0.5 wt% and one andradite crystal from Tuff 1 contains 1.5–1.7 wt% Nb_2O_5.

The andradite and schorlomite show highly variable composition within each of the marker tuffs and particularly in Tuff 1 (Fig. 16). Our new data extend the established compositional range by McHenry (2011) toward a nearly ideal andradite, and the observed spread in Fe^{3+}-Ti apfu values is much greater when compared with the andradite-schorlomite from the Sadiman nephelinites.

Perovskite occurs in all of the studied tuffs as anhedral to euhedral crystals and is often associated with magnetite (Figs. 6a and 9a, b, 10d). It has been suggested as a suitable mineral for a stratigraphic division of the marker tuffs based on major element composition (McHenry, 2011), with Ti enrichment in Tuffs 5–8 and Ti depletion in Tuffs 1–4. The analytical data for perovskite however, given by McHenry (2011) are, however, incomplete (low analytical totals) and lacking key minor elements such as REE, Nb, Sr and Th and therefore this mineral has been reinvestigated (109 spot analyses) (Table 6).

Content of the major elements, calcium and titanium, is similar to a range established by McHenry (2011) with 35.6–41.1 wt% CaO and 52.0–57.4 wt% TiO_2. The observed distribution for CaO–TiO_2 however, does not confirm previously published data (Fig. 17), e.g. all analysed crystals in the Tuff 2 show enrichment in titanium and are

compositionally similar to those from Tuff 8. The latter, in turn, contains two compositionally distinct mineral populations with both high and low TiO_2 and CaO (Fig. 17). The Augite-biotite tuff from Tuff 7 contains perovskite with a highly variable content of these elements.

Among the minor components, perovskite contain light REE (La_2O_3 to Sm_2O_3 = 0.3–5.5 wt%), Nb (0.3–3.9 wt% Nb_2O_5), Fe (0.6–2.1 wt% Fe_2O_3) and Na (0.1–1.2 wt% Na_2O). Trace elements include Th (up to 0.6 wt% ThO_2), Sr (up to 0.4 wt% SrO) and Ta (up to 0.2 wt% Ta_2O_5).

The distribution of minor elements, e.g. REE and Nb, in perovskite from individual marker tuffs is variable (Fig. 17). Data for the mineral from Tuff 2 and the white and gray tuffs from Tuff 7 form compact fields with small variations in element content. In contrast, perovskite from other studied samples display significant variations between different crystals, and within a single tuff layer, e.g. in the Augite-biotite tuff from Tuff 7 and Tuff 8.

Perovskite from Sadiman nephelinites (Nb_2O_5 = 0.6–1.6 wt% and REE_2O_3 = 2.1–4.9 wt% excluding alteration rims) is compositionally similar to perovskite from Tuff 8 and, in part, from the Augite-biotite tuff of Tuff 7 (Fig. 17).

Magnetite is a common mineral in all of the marker tuffs (Table 1) and appears to be better preserved during the original ash alteration and subsequent consolidation than the silicate minerals. Its morphology within pellets varies from anhedral to euhedral, with no sign of alteration observed (no iron hydroxides have been identified, and it also has low Si and Ca) (Figs. 6a, 9a and 10d). The magnetite has been well studied and its composition has been used for distinguishing individual marker tuffs (McHenry, 2011) and for comparison with different volcanic and plutonic rocks from Sadiman volcano (Zaitsev et al., 2015).

New data (208 spot analyses, Table 7), as well as published data (McHenry, 2011; Zaitsev et al., 2015) show that magnetite is characterised by a wide range in content of both major and minor components (Table 7, Fig. 18). Magnetite is a Ti-rich variety with TiO_2 content between 4.9 and 17.7 wt%, and is also enriched in Mg (MgO = 0.1–7.5 wt%), Al (Al_2O_3 = 0.1–3.7 wt%) and Mn (MnO = 0.3–1.7 wt%), trace elements are V (up to 0.5 wt% V_2O_3), Cr (up to 0.3 wt% Cr_2O_3) and Zn (up to 0.2 wt% ZnO).

Each marker tuff contains several compositional varieties of magnetite, and the compositional fields for magnetite from different tuffs are overlapping (Fig. 18). Several magnetite crystals from Tuffs 1, 4, 5 and 6 contain Mg and Al at levels similar to that in magnetite from Sadiman, but the majority of magnetite from the Laetolil tuffs, including Tuff 7, are high Mg and Al varieties with formulae of: $(Fe^{2+}_{0.59}Mg_{0.40}Mn_{0.01})(Fe^{3+}_{1.03}Fe^{2+}_{0.43}Ti_{0.43}Al_{0.11})O_4$ (highest Mg) and $(Fe^{2+}_{0.72}Mg_{0.26}Mn_{0.02})(Fe^{3+}_{1.30}Fe^{2+}_{0.27}Ti_{0.27}Al_{0.16})O_4$ (highest Al).

Sanidine is an uncommon mineral within marker tuffs, but was found in Tuffs 3, 6, 7 and 8. The mineral occurs as single crystals up to 500 μm in size, sometimes observed in intergrowths with clinopyroxene or containing inclusions of Na-rich clinopyroxene (3.5–6.4 wt% Na_2O) (Fig. 19). No twinning has been observed in any studied crystals. Compositionally (64 spot analyses, Table 8), sanidine is represented by a low sodium variety (0.5–0.6 wt% Na_2O in Tuff 3 and 0.9–1.7 wt% Na_2O in Tuffs 6, 7 and 8). All analyses show the presence of Ba between 0.2 and 1.9 wt% BaO with average value of 0.5 wt%.

Sanidine with a low content of the albite end-member is also known from one variety of the Sadiman nephelinites (Ab = 11.7–15.5 mol.%), but, generally, sanidine from Sadiman is more rich in Na (Ab = 13.4–42.6 mol.%) compared to the mineral from Laetoli (Ab = 4.7–14.7 mol.%) (Zaitsev et al., 2012).

5.2. Tuff geochemistry

Previously published bulk geochemical data for the Upper Laetolil marker tuffs are restricted to one sample collected "near the preserved layer of *Australopithecus afarensis* footprints" (Kasanzu et al., 2016, p. 93). In the present study, 30 samples of marker tuffs have been selected for bulk chemical analysis. The bulk-rock compositions (Table 9, 1S)

Table 5
Selected analyses of andradite and schorlomite.

Tuff	UL 1			UL 4			UL 6			UL 7			UL 8		
Sample	LA 1.20			LA 1.23			LA 1.06			LA 10E.02			LA 1.16		
Analysis	1/34	1/10	1/2	1/39	1/45	1/53	1/89	1/96	1/101	1/12	1/16	1/3	1/56	1/77	1/50
MgO	0.12	0.16	0.95	0.06	0.57	1.26	0.60	0.51	1.04	0.24	1.15	0.90	0.58	0.44	1.29
Al_2O_3	0.46	0.15	0.20	1.68	0.62	0.62	1.51	0.66	0.85	1.02	1.10	0.48	1.22	0.46	2.14
SiO_2	35.26	32.62	29.04	34.74	28.81	25.66	32.06	30.40	27.74	32.21	30.54	25.96	32.63	30.20	25.79
CaO	32.58	32.22	32.10	32.88	31.74	31.27	32.71	32.32	32.33	32.47	31.89	31.42	33.36	32.42	32.42
TiO_2	0.79	6.82	16.59	1.93	13.73	16.87	7.22	11.13	15.14	6.08	12.35	18.91	5.95	11.13	17.84
$Fe_2O_{3calc.}$	30.25	25.33	16.24	28.06	18.99	16.20	23.85	20.69	18.73	24.07	17.13	17.31	25.24	21.04	17.60
$FeO_{calc.}$	0.27	2.01	4.87	0.55	4.00	3.76	2.05	3.95	3.37	2.31	3.65	3.95	0.67	2.73	2.44
V_2O_3	0.10	0.19	0.08	0.12	0.26	0.11	0.26	0.53	0.22	0.61	0.13	0.11	0.34	0.47	
Na_2O	0.09	0.36	0.47	0.06	0.33	0.32	0.06	0.21	0.15	0.13	0.31	0.51	0.06	0.40	0.19
MnO	0.42	0.55	0.37	0.44	0.43	0.30	0.24	0.42	0.24	0.37	0.47	0.36	0.34	0.42	0.22
ZrO_2			0.35		0.37	3.07	0.38	0.33	0.65	0.28	0.50	0.48	0.09	0.41	0.86
Nb_2O_5		0.28	0.23		0.13			0.09			0.53			0.07	
Total	100.34	100.70	101.50	100.52	99.98	99.43	100.94	101.24	100.47	99.79	99.75	100.38	100.49	100.20	100.79
Si	2.967	2.750	2.435	2.906	2.457	2.225	2.683	2.555	2.355	2.731	2.520	2.217	2.735	2.560	2.180
Fe^{3+}		0.235	0.546		0.481	0.711	0.168	0.380	0.560	0.168	0.387	0.735	0.144	0.394	0.607
Al	0.033	0.015	0.020	0.095	0.062	0.063	0.149	0.065	0.085	0.102	0.093	0.048	0.121	0.046	0.213
Total	3.000	3.000	3.000	3.000	3.000	3.000	3.000	3.000	3.000	3.000	3.000	3.000	3.000	3.000	3.000
Fe^{3+}	1.916	1.373	0.479	1.766	0.738	0.346	1.334	0.929	0.637	1.368	0.706	0.377	1.448	0.949	0.513
Ti	0.050	0.432	1.046	0.121	0.880	1.100	0.454	0.703	0.967	0.388	0.846	1.214	0.375	0.710	1.134
Fe^{2+}		0.142	0.328	0.026	0.271	0.254	0.103	0.252	0.222	0.161	0.258	0.267	0.047	0.194	0.156
Mg	0.015	0.020	0.119	0.007	0.072	0.163	0.075	0.064	0.132	0.030	0.125	0.115	0.072	0.056	0.163
V	0.007	0.013	0.005	0.008	0.018	0.008	0.017	0.036	0.015	0.041	0.008	0.008	0.023	0.032	
Zr			0.014		0.015	0.130	0.016	0.014	0.027	0.012	0.026	0.020	0.004	0.017	0.035
Nb		0.011	0.009		0.005			0.003			0.020			0.003	
Mn		0.009									0.010		0.024	0.030	
Al	0.013			0.071											
Total	2.000	2.000	2.000	2.000	2.000	2.000	2.000	2.000	2.000	2.000	2.000	2.000	1.994	1.989	2.000
Ca	2.937	2.911	2.883	2.946	2.900	2.906	2.933	2.910	2.941	2.949	2.923	2.874	2.996	2.945	2.936
Mn	0.030	0.030	0.026	0.031	0.031	0.022	0.017	0.030	0.017	0.027	0.021	0.026			0.016
Na	0.015	0.059	0.076	0.010	0.055	0.054	0.010	0.034	0.025	0.021	0.056	0.084	0.010	0.066	0.031
Fe^{2+}	0.018		0.014	0.013	0.014	0.019	0.040	0.026	0.017	0.003		0.015			0.017
Total	3.000	3.000	3.000	3.000	3.000	3.000	3.000	3.000	3.000	3.000	3.000	3.000	3.006	3.011	3.000

Fe_2O_3 and FeO calculated from charge balance (8 cations and 12 O).
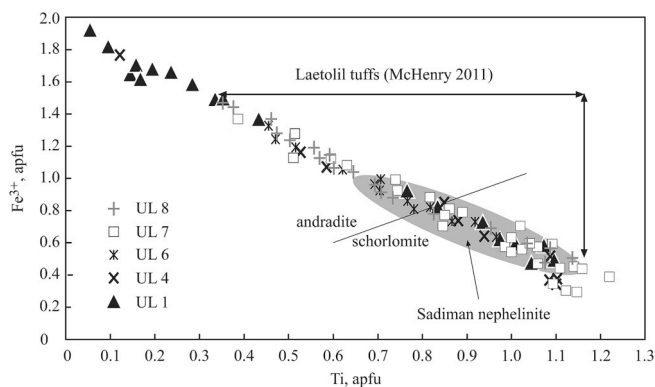
Fig. 16. Compositional variations of andradite and schorlomite. Sadiman data are from Zaitsev et al. (2012).

show that the studied tuffs are low-silica rocks (SiO_2 = 13.9–34.1 wt %), with a peralkalinity index [(Na + K)/Al in molar terms] ranging between 0.14 and 0.84, and Mg# [Mg/(Mg + Fe)] between 33 and 56. The tuffs contain high levels of Ca (17.6–39.8 wt% CaO) and volatiles (11.3–31.5 wt% CO_2, 2.0–8.9 wt% H_2O). Other major components are Fe (4.4–12.3 wt% Fe_2O_3), Al (3.9–10.7 wt% Al_2O_3), Mg (1.5–5.2 wt% MgO) and Ti (0.7–3.9 wt% TiO_2). The abundances of alkalis (Na and K) and phosphorus are typically low, with minimum values of 0.3 wt% Na_2O, 0.2 wt% K_2O and 0.4 wt% P_2O_5, but can locally reach 2.9, 3.4 and 2.2 wt%, respectively. The UL sample described by Kasanzu et al.

(2016) has lower SiO_2, Al_2O_3, Fe_2O_3 contents (11, 3.5 and 3.6 wt%, respectively) at higher CaO (40.7 wt%) compared with our data, but its precise stratigraphic position is unknown (probably a white or gray variety of Tuff 7).

The mineralogical data discussed above clearly indicate that the bulk-rock analyses of the studied marker tuff samples should not be considered representative of the primary composition of their precursor air-fall ash deposits. The tuff samples contain a significant proportion of authigenic (low-temperature secondary) calcite, montmorillonite and phillipsite. No fresh unaltered volcanic glass was preserved and primary minerals were partly or fully replaced by various secondary minerals.

On binary major-oxide diagrams (Fig. 20), the measured bulk-rock compositions form two broad fields, one of which encompasses samples high in CaO and CO_2, but low in SiO_2 (calcite-rich and silicate-poor tuffs), whereas the second field comprises high-SiO_2 and low-CaO-CO_2 values (i.e., tuffs rich in montmorillonite or primary silicates). The observed heterogeneity of the marker tuffs in texture (fine-to coarse-grained), structure (layering) and mineralogy (large variations in the proportion of primary and secondary minerals) is reflected in their variable chemical composition within a single sample of a particular marker unit (e.g., for Tuffs 1, 3, 5), as well as between different localities of the same marker unit (e.g., Tuff 8; Fig. 20, Table 1S). Variations are particularly striking within Tuff 7, which consists of four distinct layers (identified on the basis of their texture, structure and mineralogy): two upper layers enriched in Si, Al, Fe and Ti due to the presence of primary silicate minerals (Augite-biotite tuff) or montmorillonite (laminated tuff), and two lower layers (white and gray

Table 6
Selected analyses of perovskite.

Tuff	UL 1		UL 2		UL 4		UL 6		UL 7			UL 7		UL 8	
Sample	LA 1.20		LA 1.21		LA 1.23		LA 1.06		LA 10E.02			LA 1.09		LA 1.16	
Analysis	1/23	1/24	1/2	1/8	1/58	1/61	1/85	1/98	1/19	1/22	1/10	1/25	1/32	1/40	1/88
Na_2O	0.80	0.24	0.29	0.38	0.83	0.36	0.20	0.17	0.82	0.69	0.31	0.53	0.50	0.39	0.85
MgO		0.04			0.04		0.04			0.04			0.04		0.04
Al_2O_3	0.05	0.14	0.20	0.17	0.11	0.11	0.14	0.12	0.16	0.15	0.15	0.19	0.18	0.11	0.13
CaO	37.05	40.09	40.33	39.82	36.85	38.99	40.02	40.49	35.89	37.33	39.67	39.84	39.89	39.95	37.23
TiO_2	54.37	56.43	55.80	55.60	53.23	55.83	56.84	57.15	52.12	54.70	56.20	56.16	55.80	56.17	54.87
Fe_2O_3	1.23	0.92	1.56	1.37	1.56	1.03	0.99	0.89	2.04	1.16	1.03	1.33	1.47	0.92	1.04
SrO	0.37	0.12	0.14		0.20	0.17	0.09		0.26	0.09	0.10	0.09	0.14	0.08	0.17
Nb_2O_5	1.69	0.68	0.57	0.43	2.52	0.96	0.39	0.70	1.93	0.58	0.61	0.87	0.85	0.72	0.78
La_2O_3	0.64				0.15	0.14			1.35	0.21	0.09	0.08		0.09	0.51
Ce_2O_3	2.19	0.82	0.71	1.13	2.07	1.19	1.05	0.56	3.13	2.25	1.28	0.96	0.93	1.12	2.42
Pr_2O_3	0.21			0.15	0.27	0.11	0.09		0.31	0.27	0.13	0.12		0.12	0.24
Nd_2O_3	0.58	0.20	0.21	0.34	0.79	0.33	0.33	0.10	0.67	0.91	0.41	0.24	0.19	0.30	0.86
Sm_2O_3				0.07	0.09					0.12	0.07	0.08	0.05	0.07	0.12
Ta_2O_5	0.11				0.15					0.14					0.10
ThO_2	0.20			0.13	0.47	0.09	0.10			0.28	0.67	0.11	0.07		0.26
Total	99.50	99.68	99.81	99.59	99.32	99.31	100.28	100.17	98.97	99.31	100.16	100.56	100.04	100.04	99.63
Ca	0.935	0.986	0.993	0.987	0.934	0.969	0.980	0.988	0.923	0.943	0.978	0.978	0.983	0.985	0.939
Na	0.006	0.002	0.002	0.003	0.006	0.003	0.001	0.001	0.006	0.005	0.002	0.004	0.004	0.003	0.007
Sr	0.005	0.002	0.002		0.003	0.002	0.001		0.004	0.001	0.001	0.001	0.002	0.001	0.002
La	0.006				0.001	0.001			0.012	0.002	0.001	0.001		0.001	0.004
Ce	0.019	0.007	0.006	0.010	0.018	0.010	0.009	0.005	0.027	0.019	0.011	0.008	0.008	0.009	0.021
Pr	0.002			0.001	0.002	0.001	0.001		0.003	0.002	0.001	0.001		0.001	0.002
Nd	0.005	0.002	0.002	0.003	0.007	0.003	0.003	0.001	0.006	0.008	0.003	0.002	0.002	0.002	0.007
Sm				0.001	0.001					0.001	0.001	0.001		0.001	0.001
Th	0.001			0.001	0.003		0.001		0.002	0.004	0.001				0.001
Total	0.978	0.998	1.005	1.005	0.974	0.989	0.996	0.994	0.982	0.986	0.998	0.995	0.998	1.003	0.984
Ti	0.963	0.975	0.965	0.968	0.947	0.974	0.978	0.979	0.941	0.970	0.973	0.968	0.965	0.972	0.971
Fe^{3+}	0.022	0.016	0.027	0.024	0.028	0.018	0.017	0.015	0.037	0.021	0.018	0.023	0.025	0.016	0.018
Nb	0.018	0.007	0.006	0.004	0.027	0.010	0.004	0.007	0.021	0.006	0.006	0.009	0.009	0.007	0.008
Al	0.001	0.004	0.005	0.005	0.003	0.003	0.004	0.003	0.005	0.004	0.004	0.005	0.005	0.003	0.004
Mg		0.001			0.001		0.001			0.001			0.001		0.001
Ta	0.001				0.001					0.001					0.001
Total	1.005	1.003	1.003	1.000	1.007	1.005	1.004	1.005	1.003	1.004	1.001	1.005	1.006	0.999	1.004
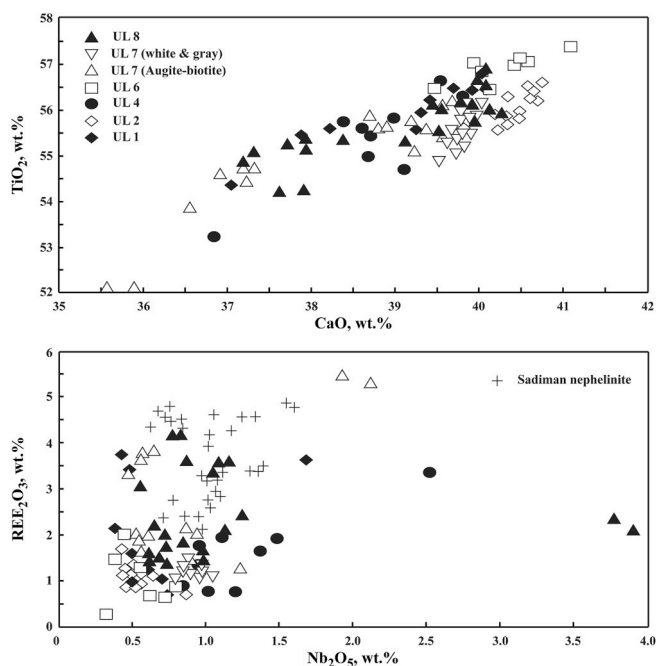
Fig. 17. Compositional variations of the perovskite. Sadiman data are from Zaitsev et al. (2012).

tuffs) both enriched in Ca and C due to the abundance of calcite coupled with a relatively low content of silicate minerals (Table 9, Fig. 20).

The trace-element distributions within the studied marker tuffs are characterised by highly variable contents (all in ppm) of Ba (84–2768), Sr (635–2576), REE (176–957), Cu (97–604), Zr (70–395), V (25–379), Nb (30–220), Zn (81–206) and Rb (6–104). Other elements are present, but at lower levels (< 50 ppm). Accurate interpretation of the trace-element geochemical data for the marker tuffs is problematic because they consist of a complex mixture of minerals of different origin. The high Ba content in the studied samples, for example, is related to the presence of secondary baryte and Mn–Ba hydroxide, which, along with calcite, may also contains significant levels of Sr. There is also no doubt that some elements were mobile during the tuff alteration. However, multi-element distribution patterns normalized to the primitive mantle composition, which are typically used for the characterization of volcanic rocks, show a similar pattern for nearly all of the studied samples (Fig. 4S). Of particular note are distinct negative anomalies (troughs) at Rb, Ta, K, Hf and Ti, coupled with positive anomalies (spikes) at U, Pb and Sr.

The greatest element variations within a single marker unit are observed for well-stratified Tuff 7 (Table 9, Fig. 21), where the three types of tuff can be precisely identified on the basis of their element abundances, distribution patterns and/or selected element ratios. The upper Augite-biotite tuff is characterised by high Th content, with the highest recorded Th/U ratio (2.6–3.9), high Ce/Pb ratio (39–105), a pronounced negative Pb anomaly, and low Nb/Ta values (12–31). In contrast, the underlying laminated tuff is enriched in U and is characterised by the lowest recorded Th/U and Ce/Pb ratios (0.10–0.13 and

Table 7
Selected analyses of magnetite.

Tuff	UL 1			UL 2	UL 3	UL 4		UL 5		UL 6		UL 7		UL 8	
Sample	LA 1.20			LA 1.21	LA 1.22	LA 1.23		LA 1.24		LA 1.06		LA 1.09		LA 1.16	
Analysis	13	8	30	4	40	3	13	71	91	3	13	4	8	30	20
MgO	0.30	2.47	6.22	5.16	7.49	0.70	3.21	2.53	6.69	1.00	3.95	2.64	6.59	1.79	4.41
Al_2O_3	0.05	1.89	2.12	3.47	2.96	0.81	3.50	2.58	2.55	0.40	3.16	2.25	2.52	1.83	2.54
SiO_2	0.07	0.04	0.02	0.02	0.06	0.04	0.03	0.03	0.04	0.04	0.04	0.06	0.05	0.03	0.05
CaO	0.03	0.03	0.05	0.16	0.08	0.02		0.10	0.09	0.08	0.06	0.07	0.05	0.04	0.03
TiO_2	6.37	10.02	13.58	9.65	13.49	5.63	9.49	9.44	16.49	8.24	9.84	9.51	15.03	10.23	15.53
Fe_2O_{3calc}	56.80	48.82	43.55	49.30	43.77	57.49	48.36	48.74	37.11	52.84	48.44	48.90	40.39	48.01	38.30
$FeO_{calc.}$	35.73	36.28	33.62	32.11	32.31	34.88	35.05	35.49	35.84	36.27	34.14	35.45	34.90	37.43	38.64
V_2O_3	0.36	0.19	0.15	0.11	0.10	0.26	0.13	0.13	0.14	0.35	0.17	0.15	0.10	0.19	0.17
Cr_2O_3	0.05	0.02	0.05		0.03	0.04	0.02		0.19	0.04	0.03	0.03		0.02	0.06
MnO	1.05	0.75	0.84	0.53	0.45	0.59	0.59	0.66	0.49	0.99	0.61	0.67	0.44	0.72	0.58
ZnO	0.05	0.04	0.05	0.05	0.04	0.06	0.08	0.08	0.04		0.04			0.07	0.07
Total	100.86	100.55	100.25	100.56	100.77	100.53	100.46	99.77	99.67	100.25	100.48	99.74	100.08	100.36	100.39
Fe^{2+}	0.948	0.840	0.642	0.707	0.593	0.940	0.806	0.838	0.628	0.912	0.767	0.833	0.637	0.876	0.743
Mg	0.017	0.136	0.332	0.276	0.392	0.039	0.174	0.139	0.356	0.056	0.213	0.146	0.350	0.099	0.237
Mn	0.034	0.023	0.025	0.016	0.013	0.019	0.018	0.021	0.015	0.032	0.019	0.021	0.013	0.023	0.018
Zn	0.001	0.001	0.001	0.001	0.001	0.002	0.002	0.002	0.001		0.001			0.002	0.002
Total	1.000	1.000	1.000	1.000	1.000	1.000	1.000	1.000	1.000	1.000	1.000	1.000	1.000	1.000	1.000
Fe^{3+}	1.617	1.353	1.173	1.329	1.157	1.632	1.324	1.356	0.996	1.500	1.320	1.362	1.083	1.340	1.039
Ti	0.181	0.278	0.365	0.260	0.356	0.160	0.260	0.263	0.442	0.234	0.268	0.265	0.403	0.286	0.421
Fe^{2+}	0.183	0.278	0.364	0.255	0.356	0.160	0.261	0.260	0.440	0.232	0.267	0.264	0.403	0.285	0.422
Al	0.002	0.082	0.089	0.146	0.123	0.036	0.150	0.112	0.107	0.018	0.135	0.098	0.106	0.080	0.108
V	0.011	0.006	0.004	0.003	0.003	0.008	0.004	0.004	0.004	0.011	0.005	0.004	0.003	0.006	0.005
Cr	0.001	0.001	0.001		0.001	0.001	0.001		0.005	0.001	0.001	0.001		0.001	0.002
Si	0.003	0.001	0.001	0.001	0.002	0.002	0.001	0.001	0.001	0.002	0.001	0.002	0.002	0.001	0.002
Ca	0.001	0.001	0.002	0.006	0.003	0.001		0.004	0.003	0.003	0.002	0.003	0.002	0.002	0.001
Total	2.000	2.000	2.000	2.000	2.000	2.000	2.000	2.000	2.000	2.000	2.000	2.000	2.000	2.000	2.000

Fe_2O_3 and FeO calculated from charge balance (3 cations and 4 O).
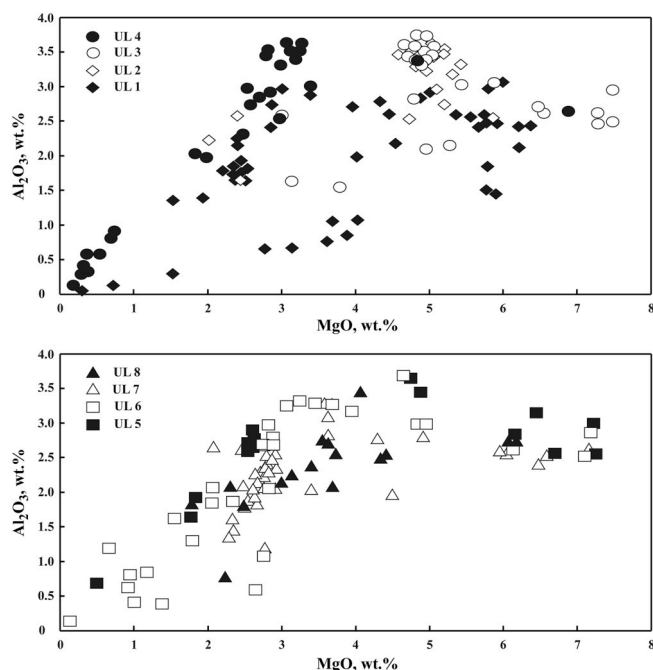
Fig. 18. Compositional variations of the magnetite.

~10, respectively), enrichment in Pb, and a clear positive Pb anomaly on its multi-element diagram. The compositions of the white and gray tuffs (bottom part of Tuff 7) are almost identical and differ from those of the Augite-biotite and laminated tuffs, even though some compositional overlap does exist: e.g., Nb/Ta values for the laminated and white-gray tuffs are 68 and 43–94, respectively. Samples from both white and gray tuffs have low Th/U and Ce/Pb ratios (0.16–0.60 and 10–19, respectively), and exhibit a positive Pb anomaly.

Fig. 21 also shows the normalized element distributions for the nephelinites and tuffs from the Sadiman volcano (Zaitsev et al., 2012). Sadiman is still considered as the likely source of the Laetolil tuffs, and the Zr/Nb ratio was used to discriminate among rocks from the Sadiman, Oldeani and Lemagarut volcanoes, and Laetoli (Fig. 8 in Kasanzu et al., 2016). There is a similarity in element patterns between the Laetoli and Sadiman rocks, with the exception of Cs, Rb, K and P. Low K, Rb and Cs values in the Laetoli samples can be explained by leaching of these elements during nepheline alteration, and the high P content is due to the relative abundance of apatite in the tuffs. The Sadiman rocks are also characterised by high Ba contents, but this is a primary feature arising from enrichment of igneous K feldspars in this element. In contrast, sanidine is relatively rare in the Laetolil tuffs and contains less Ba. Our geochemical data (Table 9 and 1S) also demonstrate a large spread in Zr/Nb ratio (1–11), which therefore cannot be used to discriminate between the Laetoli rocks and nearby volcanoes, as suggested by Kasanzu et al. (2016).

The marker tuffs contain 176–957 ppm REE and show similar chondrite-normalized REE patterns that are essentially parallel to one another. The tuffs are relatively enriched in light REE, with a $(La/Yb)_{CN}$ ratio of 18–86. Within Tuff 7, the distribution of REE is slightly different among the individual layers (Fig. 22). The Augite-biotite, laminated, and white/gray tuffs can be distinguished on the basis of element patterns and the chondrite-normalized element ratios.

5.3. Melt inclusions

Previous study of magnetite from Tuff 7 revealed the presence of rare melt inclusions with silicate glass and a carbonate phase (Fig. 6 in Zaitsev et al., 2015). In addition to magnetite, glassy inclusions (1–45 × 22 μm in size) have been also found in clinopyroxene, garnet
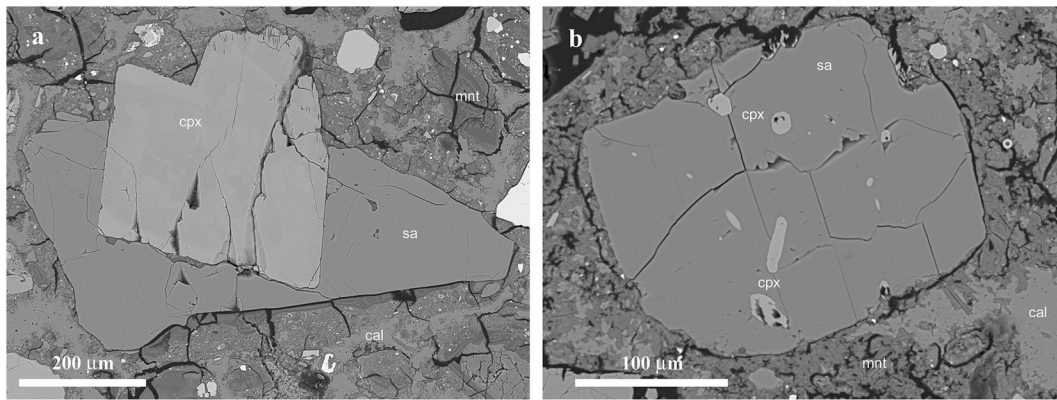
Fig. 19. Crystals of sanidine with diopside (a) and aegirine-augite (b). BSE images. For mineral symbols see Table 1.

Table 8
Selected analyses of sanidine.

Tuff	UL 3	UL 6		UL 7		UL 8	
Sample	LA 1.23	LA 1.06		LA 10E.02		LA 1.16	
Analysis	1/3	1/15	1/25	1/26	1/59	1/63	1/73
SiO_2	64.15	63.52	64.43	64.14	64.65	64.09	64.09
Al_2O_3	18.60	18.64	18.56	19.03	18.80	18.92	18.61
Fe_2O_3	0.65	0.58	0.47	0.10	0.54	0.45	0.67
Na_2O	0.57	0.96	1.37	1.14	1.65	1.43	1.32
K_2O	16.55	15.72	15.38	15.56	14.97	14.93	15.24
BaO	0.43	0.57	0.43	0.53	0.33	0.90	0.78
Total	100.95	99.99	100.64	100.50	100.94	100.72	100.71
Si	2.963	2.957	2.971	2.961	2.965	2.957	2.961
Al	1.013	1.023	1.009	1.036	1.016	1.029	1.013
Fe^{3+}	0.023	0.020	0.016	0.003	0.019	0.016	0.023
Total	3.998	4.000	3.996	4.000	4.000	4.001	3.998
K	0.975	0.934	0.905	0.916	0.876	0.879	0.898
Na	0.051	0.087	0.122	0.102	0.147	0.128	0.118
Ba	0.008	0.010	0.008	0.010	0.006	0.016	0.014
Total	1.034	1.031	1.035	1.028	1.029	1.023	1.031

and perovskite. They have a simple phase composition (Fig. 23) and consist of glass, glass + gas or glass + gas + a carbonate globule; rare daughter minerals are chalcopyrite, apatite, melilite, an unidentified Fe-bearing carbonate (possibly siderite), and Na–Ca aluminosilicate (possibly feldspathoid).

Energy-dispersive analyses (Table 10) show that glass is silica-undersaturated (SiO_2 = 30.2–45.6 wt%) and peralkaline, with a (Na + K)/Al ratio of 1.7–2.8 (Na_2O + K_2O = 8.9–18.3 wt% and Al_2O_3 = 7.9–13.6 wt%). Silicate glass in inclusions hosted by different minerals is characterised by significant differences in major-element composition. Inclusions in magnetite contain glass with the highest Mg and Ca (2.0–3.2 and 10.0–18.2 wt% respective oxides), but lowest Fe and K contents (6.6–12.4 and 3.2–5.1 wt% respective oxides). Glass from inclusions hosted by garnet shows enrichment in Si, Fe and K (SiO_2 = 44.2–45.6 wt%; Fe_2O_3 = 12.8–13.2 wt% and K_2O = 7.0–7.3 wt%) and depletion in Ca and Mg (4.2–4.5 and 0.6–0.8 wt% respective oxides). Clinopyroxene contains glass of intermediate composition (Table 10).

Carbonate phases always occur as globules (up to 6.5 μm in diameter) and are morphologically similar to those documented in melt inclusions from Oldoinyo Lengai minerals (Mitchell, 2009; Mitchell and Dawson, 2012; Sharygin et al., 2012). The globules are highly variable in composition (Table 11); e.g., SiO_2 varies from 5.8 to 26.4 wt%, CaO from 19.1 to 31.7 wt%, and Na_2O + K_2O from 9.5 to 19.6 wt%. High SiO_2, Al_2O_3 and Fe_2O_3 values detected in some of the small globules

(< 3 μm in diameter) can be explained by analytical signal coming from the host silicate glass during EDS analysis. These globules also contain lower levels of alkalis (Na and K) and volatiles (P, S, Cl and F) than globules with a low SiO_2 content. The (Na + K)/Al ratio of carbonate phases ranges between 24 (globule with the lowest Si, Al and Fe abundances) and 1.7 (globule with the highest Si, Al and Fe values). The Na/K ratio is 3.1–8.6 and the Ca/(Na + K) ratio, considered to indicate how close the globule is to natrocarbonatite, is 0.8–1.8, with an average value of 1.3.

Both silicate glasses and carbonate globules contain volatile components P, S, Cl and F (Tables 10 and 11). In general, the carbonate phase is more enriched in these elements compared with its host silicate glass. Silica-poor globules (up to 10 wt% SiO_2) contain 3.2–4.3 wt% P_2O_5, 2.8–3.9 wt% SO_3, 0.7–2.7 wt% F and 0.2–1.0 wt% Cl. All analyses have relatively low totals, i.e. 84–98 wt% for the silicate glass and 62–78 wt% for the carbonate phase. This deficiency suggests the presence of other volatile components, probably CO_2.

A Raman spectroscopic study of silicate glass and carbonate globules in five inclusions did not reveal any bands between 3000 and 4000 cm^{-1}, implying that neither H_2O nor (OH)$^-$ groups are present in the melt inclusions. The Raman spectra of glass and globules show a strong band between 1074 and 1089 cm^{-1} (Fig. 24), which can be assigned to $\nu_1(CO_3)^{2-}$ vibrations. Two relatively weak bands are observed at 950-962 cm^{-1} and 996-998 cm^{-1}, and are attributed to $\nu_1(PO_4)^{3-}$ and $\nu_1(SO_4)^{2-}$ vibrations, respectively (Zaitsev et al., 2009, 2010; Golovin et al., 2015, 2017).

The geometry of the $\nu_1(CO_3)^{2-}$ band is rather complex, and at least four different types of spectra can be identified (Fig. 24). Types I and II are observed in the spectra of silicate glasses, whereas types I, III and IV are detected in the carbonate globules. Type I is a wide band with two overlapping peaks at 1074-1075 cm^{-1} and 1088 cm^{-1} (Fig. 24a, c). Type II is also a wide band of similar shape with a main peak at 1076 cm^{-1} and a weak shoulder at 1086-1087 cm^{-1} (Fig. 24b). Type III shows a strong peak at 1089 cm^{-1} and a shoulder at 1078 cm^{-1} (Fig. 24d). Type IV is quite different from the other three and comprises a single strong and narrow peak at 1085 cm^{-1} (Fig. 24e). Comparison with published data for Na–K–Ca carbonates (Zaitsev et al., 2009, 2010; Golovin et al., 2015, 2017) suggests that the Raman spectra of type IV are related to the presence of calcite within the carbonate globules. Other spectrum types could indicate the presence of Na–K–Ca carbonates similar to nyerereite, ideally $(Na,K)_2Ca(CO_3)_2$ (Golovin et al., 2017). Shortite, another anhydrous Na–Ca carbonate, has a distinct Raman spectrum with two strong peaks at 1071 and 1090 cm^{-1} (Zaitsev and Chakhmouradian, 2002).

5.4. Sr and Nd isotopes

Previously published radiogenic isotopic compositions available for the Laetolil sequence are restricted to Sr data for one sample from the

Table 9
Major and trace element composition of the Tuff 7.

Locality	1	16	8													
Site			OFP I	OFP I	NFP II	OFP I	NFP I	NFP II	S II	OFP I	NFP I	NFP II	S II	OFP I	NFP II	S II
Tuff	Augite-biotite			laminated		white				gray						
Sample	LA 1.10	LA 16.05	1	2 c	2	2	4 a	3	1 a	2 a	4 b	3 a	1 b	2 b	3 b	2
SiO_2, wt.%	29.71	27.42	28.49	30.54	28.43	15.31	19.47	17.57	13.86	20.17	21.49	18.69	19.78	16.94	18.13	15.46
TiO_2	2.37	2.68	3.88	1.49	1.39	0.66	1.03	1.03	0.73	0.90	0.98	0.92	0.92	0.78	0.86	0.76
Al_2O_3	9.95	8.66	8.01	9.12	8.81	4.35	5.43	5.09	3.89	5.80	6.40	5.71	6.12	4.70	5.04	4.50
Fe_2O_3	10.07	10.47	12.28	10.18	9.58	4.47	6.05	5.95	4.41	6.24	6.95	6.29	6.74	6.07	6.65	5.92
CaO	24.34	25.92	24.67	20.56	24.33	39.31	34.77	36.12	39.77	33.50	32.09	34.18	32.16	36.75	35.78	37.28
MgO	3.87	3.79	4.98	2.55	2.34	1.60	1.95	1.87	1.56	1.92	1.85	1.70	1.82	1.72	1.66	1.54
MnO	0.16	0.17	0.15	0.26	0.28	0.07	0.13	0.12	0.06	0.17	0.17	0.16	0.13	0.18	0.20	0.11
Na_2O	2.58	2.20	1.64	1.89	1.04	0.87	0.60	0.64	0.67	1.15	0.70	0.66	0.92	0.98	0.76	0.77
K_2O	0.98	0.88	0.63	0.44	0.43	0.15	0.22	0.25	0.23	0.24	0.23	0.25	0.25	0.19	0.56	0.18
P_2O_5	0.42	0.71	0.61	2.01	1.73	0.70	0.77	0.83	0.69	0.84	1.01	0.84	0.72	0.75	0.87	1.05
CO_2	14.08	15.98	12.01	14.16	17.16	30.05	26.16	27.77	31.53	25.52	24.16	26.42	25.63	28.14	27.39	29.25
H_2O	2.87	2.56	2.85	4.41	3.85	3.17	2.69	2.29	2.00	2.95	2.79	3.30	2.72	2.73	2.50	2.08
Total	101.42	101.45	100.20	97.60	99.37	100.71	99.29	99.51	99.40	99.39	98.83	99.12	97.93	99.92	100.41	98.91
$(Na + K)/Al$	0.53	0.53	0.42	0.39	0.25	0.37	0.23	0.26	0.35	0.37	0.22	0.24	0.29	0.39	0.37	0.33
Mg#	46.4	44.8	47.7	36.1	35.4	44.5	42.0	41.5	44.3	40.9	37.4	37.8	37.8	38.9	35.9	37.0
Li, ppm	13.1	14.0	na	na	na	na	na	na	na	na	na	na	na	na	na	na
Be	3.82	4.14	na	na	na	na	na	na	na	na	na	na	na	na	na	na
Sc	12.0	15.2	20.5	3.91	4.10	2.85	4.70	4.57	3.51	2.63	3.24	3.25	2.47	1.97	2.19	2.70
V	249	261	202	66.2	83.5	24.5	53.2	59.7	41.2	48.2	45.2	47.7	46.1	41.5	51.1	35.3
Cr	na	na	10.0	< 2	< 2	< 2	4.08	4.50	4.09	< 2	< 2	< 2	< 2	< 2	< 2	< 2
Co	34.4	39.1	36.9	28.0	30.8	8.19	19.3	17.7	8.17	21.4	19.8	18.2	18.1	19.3	20.9	15.1
Ni	8.13	10.06	10.2	3.55	4.69	1.61	3.84	3.09	2.64	3.48	2.69	2.50	2.51	2.83	3.36	2.08
Cu	97	121	152	604	593	241	295	291	205	327	266	251	239	218	262	164
Zn	121	143	109	204	178	87.4	111	101	81.0	156	129	116	136	149	148	123
Rb	25.6	27.9	17.0	16.5	17.3	5.96	9.80	10.6	9.67	9.46	10.1	10.5	10.0	6.81	20.7	6.89
Sr	635	819	924	1495	1184	1528	1063	966	1624	1315	924	846	1181	1435	1105	1364
Y	33.9	33.5	29.3	51.6	51.1	21.3	26.7	25.9	18.9	33.9	29.5	26.1	25.8	30.2	33.1	26.1
Zr	395	355	261	364	357	162	183	184	152	189	201	182	70.1	158	170	175
Nb	36.8	64.4	201	208	220	95.7	94.9	85.3	79.2	120	130	113	42.8	97.3	129	109
Mo	0.12	0.21	0.14	2.97	1.02	0.48	0.23	0.27	0.10	2.75	0.30	0.41	0.27	2.44	0.69	0.18
Cd	0.18	0.14	0.12	0.15	0.22	0.24	0.22	0.19	0.22	0.25	0.20	0.10	0.21	0.22	0.19	0.32
Sn	2.70	2.41	2.13	2.03	2.24	0.89	0.75	0.61	1.00	1.16	0.96	0.68	0.65	1.06	1.21	0.80
Sb	0.16	0.13	< 0.16	0.27	0.33	< 0.16	0.20	0.17	< 0.16	0.22	0.21	0.17	0.17	0.18	0.23	0.16
Cs	0.22	0.24	< 0.01	< 0.01	< 0.01	0.03	0.09	0.13	0.13	< 0.01	0.05	0.08	< 0.01	< 0.01	< 0.01	0.04
Ba	179	260	457	187	258	136	147	187	1310	106	84	155	96	172	323	127
Hf	4.44	2.42	7.89	7.55	7.69	3.46	3.91	3.85	3.07	3.76	4.08	3.67	0.85	3.16	3.33	3.13
Ta	1.20	2.45	16.37	3.07	3.25	1.01	2.21	1.86	1.47	1.92	2.01	1.84	0.596	1.72	2.14	1.71
Pb	4.12	5.58	4.24	17.4	17.3	3.39	8.44	8.51	3.08	12.2	9.97	9.64	8.83	14.3	14.8	9.98
Th	7.47	19.5	31.9	2.40	2.36	1.05	3.57	3.73	1.78	2.06	1.97	2.23	1.77	2.34	2.73	1.81
U	2.84	6.07	8.19	22.9	17.5	6.52	5.97	7.55	4.16	9.11	7.16	7.22	4.59	8.75	8.80	5.21
La, ppm	91.4	142	222	158	155	61.5	87.3	87.9	56.9	107	94.9	85.5	77.5	110	134	101
Ce	161	276	445	179	177	64.6	122	125	69.2	134	117	117	108	139	152	112
Pr	17.0	30.2	47.6	15.2	14.8	6.6	11.1	11.5	6.89	11.5	10.2	9.9	9.27	11.6	12.9	9.51
Nd	61.6	108.0	171	50.0	49.3	21.4	37.6	39.0	23.0	37.3	34.3	32.6	30.8	37.1	41.5	31.9
Sm	11.4	17.6	26.9	10.7	10.4	4.50	7.36	7.47	4.64	7.69	6.76	6.46	6.52	7.10	7.87	5.72
Eu	3.59	5.02	7.23	3.83	3.79	1.62	2.42	2.45	1.57	2.65	2.38	2.21	2.21	2.40	2.63	1.98
Gd	10.0	12.9	18.7	12.7	12.5	5.27	7.54	7.48	4.96	8.63	7.56	7.02	7.06	7.63	8.29	6.30
Tb	1.47	1.72	2.12	1.86	1.85	0.766	1.05	1.05	0.707	1.23	1.11	0.999	1.02	1.09	1.19	0.883
Dy	8.00	8.62	10.1	11.1	10.9	4.58	6.11	5.94	4.18	7.27	6.42	5.77	5.83	6.28	6.79	5.23
Ho	1.40	1.44	1.48	1.99	1.98	0.813	1.07	1.04	0.734	1.30	1.16	1.03	1.02	1.09	1.23	0.921
Er	3.55	3.48	3.16	5.19	5.20	2.10	2.67	2.67	1.89	3.37	2.98	2.63	2.63	2.93	3.23	2.45
Tm	0.463	0.436	0.348	0.658	0.664	0.266	0.340	0.328	0.238	0.415	0.371	0.333	0.331	0.375	0.412	0.309
Yb	2.69	2.55	1.84	3.91	3.84	1.60	1.97	1.91	1.43	2.45	2.16	1.88	1.88	2.13	2.41	1.82
Lu	0.384	0.359	0.247	0.513	0.506	0.211	0.260	0.252	0.195	0.324	0.285	0.253	0.247	0.291	0.335	0.241
Total	374	611	957	454	447	176	289	294	177	325	288	273	254	329	376	280
Th/U	2.62	3.21	3.89	0.10	0.13	0.16	0.60	0.49	0.43	0.23	0.28	0.31	0.39	0.27	0.31	0.35
Ce/Pb	39.0	49.5	104.9	10.3	10.2	19.0	14.4	14.7	22.5	11.0	11.7	12.1	12.2	9.7	10.3	11.2
Nb/Ta	30.6	26.3	12.3	67.8	67.8	94.3	43.0	45.8	53.7	62.7	64.8	61.4	71.9	56.5	60.1	63.8
Zr/Nb	10.7	5.51	1.30	1.75	1.62	1.69	1.93	2.15	1.92	1.57	1.55	1.61	1.64	1.62	1.32	1.60
$(La/Ce)_{CN}$	1.47	1.33	1.29	2.28	2.26	2.46	1.85	1.81	2.12	2.06	2.09	1.89	1.86	2.04	2.28	2.32
$(La/Yb)_{CN}$	24.3	40.0	86.3	29.0	28.9	27.5	31.8	33.1	28.6	31.3	31.5	32.6	29.5	37.1	40.0	39.7
$(La/Lu)_{CN}$	25.5	42.6	96.1	33.0	32.8	31.2	35.9	37.3	31.2	35.3	35.7	36.2	33.7	40.5	43.0	44.8
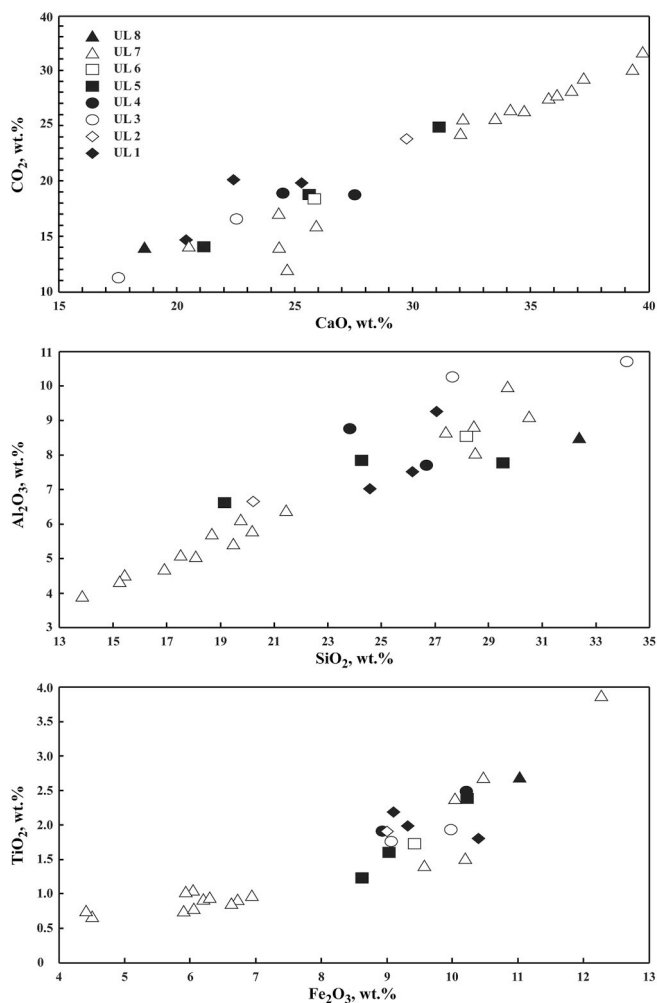
Fig. 20. Major element variations in the marker tuffs.

Fig. 21. Primitive mantle-normalized plots for Tuff 7, and Sadiman nephelinites and tuffs. Data for Sadiman are from Zaitsev et al. (2012), normalizing values for primitive mantle are from Sun and McDonough (1989).

Lower Laetolil tuff and another one from the Upper Laetolil tuff (Kasanzu et al., 2016). The former sample is the same material that was analysed geochemically (see above). Kasanzu et al. (2016) determined $^{87}Sr/^{86}Sr$ ratios only and did not report $^{87}Rb/^{86}Sr$ values. In this study, we analysed eight samples from Tuffs 6, 7 and 8 for Sr and Nd isotopic composition (Table 12). An acid-soluble and an insoluble fractions were analysed for each of the samples. We assume that the measured isotopic composition of the soluble fraction is controlled by calcite (for both Sr and Nd), phillipsite (for Nd, Campbell et al., 2012) and montmorillonite (for both Sr and Nd, Hay, 1978, Chaudhuri and Brookins, 1979; Takahashi et al., 2004, van der Watt and Waanders, 2012). For the insoluble fraction, both Sr and Nd budgets are controlled by common primary silicate minerals (clinopyroxene, garnet, nepheline, titanite), perovskite and apatite. The Rb–Sr and Sm–Nd data are given in Table 12, where the measured $^{87}Sr/^{86}Sr$ and $^{143}Nd/^{144}Nd$ values were corrected for an age of 3.66 Ma.

The leached fractions contain 2.58–21.6 ppm Rb, 956–2059 ppm Sr, 2.82–11.9 ppm Sm, 16.1–65.5 ppm Nd; the measured $^{87}Rb/^{86}Sr$ and $^{147}Sm/^{144}Nd$ ratios are 0.0045–0.0572 and 0.0988–0.1477, respectively. In comparison with the acid-soluble material, the residual fraction is generally enriched in Rb (13.6–103.4 ppm), although one sample contains slightly lower Rb. The insoluble fraction invariably contains less Sr (124–242 ppm) and, hence, is characterised by much higher $^{87}Rb/^{86}Sr$ ratios (0.2263–1.7020). The Sm–Nd budgets of the two fractions do not show such a straightforward relationship. In the insoluble material, Sm values range from 2.05 to 22.9 ppm, Nd from 11.2 to 140 ppm and $^{147}Sm/^{144}Nd$ ratios from 0.0938 to 0.1441, i.e. can be
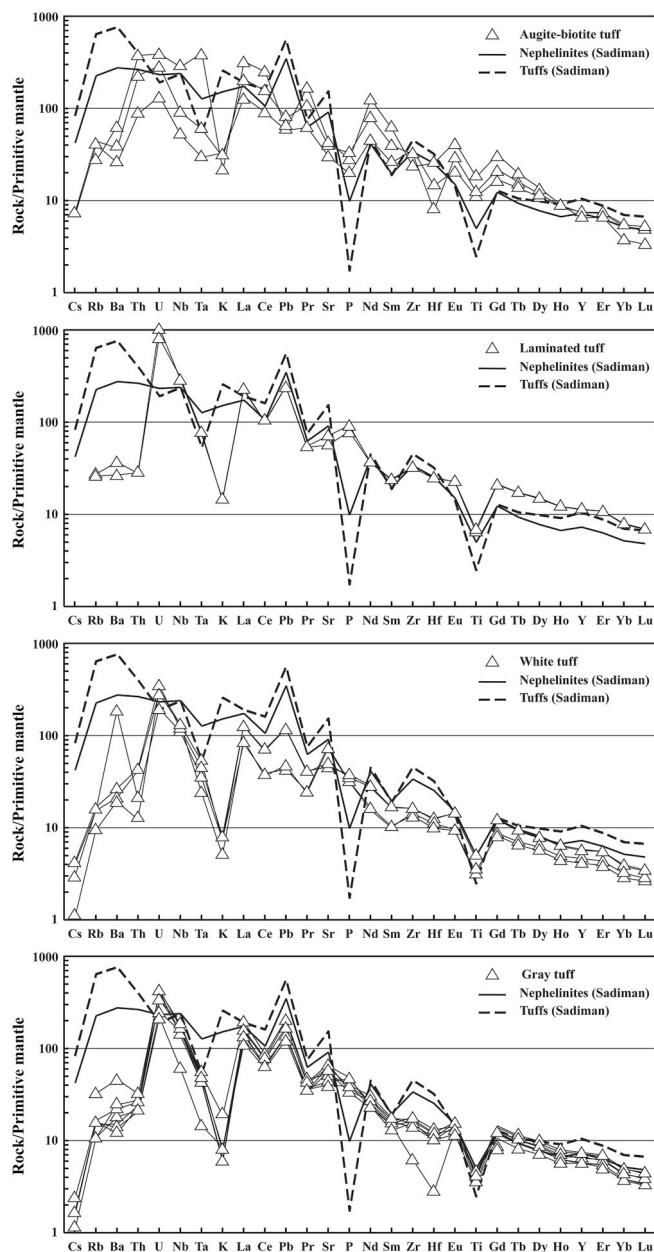
either higher or lower than those in the leached fraction (Table 12).

Because of the young age of the Laetolil tuffs, the age-corrected initial $^{143}Nd/^{144}Nd$ ratios differ from the measured ones by 0.000002–0.000004; these values are below the calculated 2σ (0.000003–0.000009). The measured and initial $^{87}Sr/^{86}Sr$ ratios are essentially identical in the leached fraction (their difference being < 0.000003), whereas the $^{87}Sr/^{86}Sr$ initial ratios in the Rb-rich, Sr-poor residual fraction are significantly lower than the measured values (by 0.00001–0.00009). The published Sr and Nd isotopic data for different volcanic rocks from the Laetoli area, Olduvai Gorge, Crater Highlands and Gregory Rift are restricted to $^{87}Sr/^{86}Sr$ and $^{143}Nd/^{144}Nd$ ratios only (Mollel et al., 2008, 2009; 2011; Mana et al., 2012, 2015; Kasanzu et al., 2016). Our data for Laetolil tuffs, as well as unpublished data for nephelinites from the Sadiman volcano, show that the knowledge of Rb–Sr isotopic budget is essential for the comprehensive understanding of genetic relations between volcanic silicate rocks and volcaniclastic
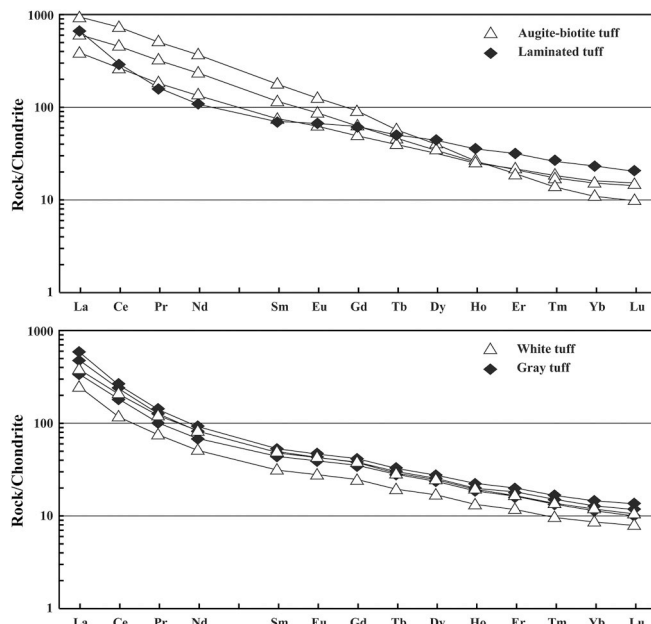
Fig. 22. Chondrite-normalized plots for Tuff 7. Normalizing values for chondrite are from Sun and McDonough (1989).
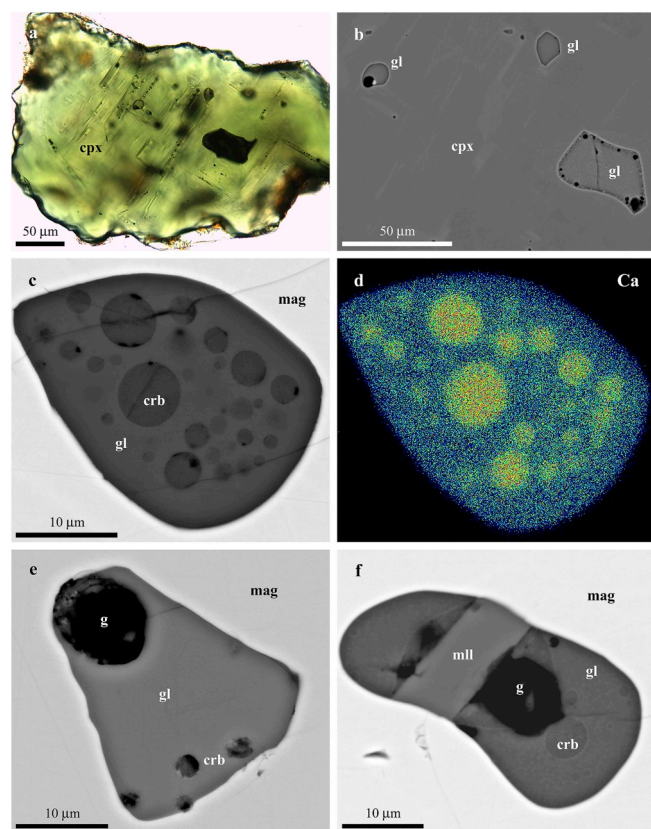

Fig. 23. Melt inclusions in diopside and magnetite from the white tuff of Tuff 7. gl – silicate glass, g – gas, crb – carbonate globule. (a) Transmitted light, (b, c, e, and f) BSE images, (d) X-ray Ca distribution map. (b) detail of (a). For mineral symbols see Table 1.

materials, even if their age is young by geological standards.

The calculated initial $^{87}Sr/^{86}Sr$ and $^{143}Nd/^{144}Nd$ ratios are shown in Fig. 25, including tie-lines connecting the leached and residual fractions for each sample. For comparison, we also plotted the available

published and unpublished Sr–Nd data for the Sadiman, Mosonik and Essimingor volcanoes (Paslick et al., 1995, 1996, Mollel et al., 2011; Mana et al., 2012, Zaitsev et al. unpubl.). Both leached and residual fractions from the Laetolil tuffs show a wide variation in Sr and Nd isotopic ratios. The magnitude of variation is greater for the residual fractions ($^{87}Sr/^{86}Sr$ = 0.70364–0.70543, $^{143}Nd/^{144}Nd$ = 0.51259–0.51278) relative to the acid-soluble material ($^{87}Sr/^{86}Sr$ = 0.70427–0.70505, $^{143}Nd/^{144}Nd$ = 0.51250–0.51274).

The samples from individual tuff units show quite different Sr–Nd isotopic budgets (Fig. 25). Thus, Tuff 6 is characterised by a lower Nd isotopic ratio compared to the other tuffs; its leached fraction has the lowest $^{143}Nd/^{144}Nd$ ratio (0.51250) among the studied samples. Samples from Tuffs 7 and 8 show relatively little variation in $^{143}Nd/^{144}Nd$ (0.51266–0.51278), but their $^{87}Sr/^{86}Sr$ values are highly variable (0.70364–0.70543). The minimum and maximum Sr isotopic ratios were obtained for residual fractions from Tuff 7 (Augite-biotite unit) and Tuff 8, respectively. The laminated, white and gray layers of Tuff 7 have intermediate Sr isotopic compositions. The $^{87}Sr/^{86}Sr$ values of residual fractions from the white and gray tuffs are identical (0.70454–0.70455), whereas the laminated tuff has a slightly lower ratio (0.70444). Leached fractions from Tuffs 7 and 8 have similar $^{143}Nd/^{144}Nd$ ratios (0.51267–0.51272) and very variable $^{87}Sr/^{86}Sr$ values (0.70427–0.70485).

The relationship between the Sr and Nd ratios of the two analysed fractions within the same sample also differs across the examined sample suite (Fig. 25). Between the residual and leached fractions, we observe: (1) a shift to lower Nd and slightly higher Sr isotopic ratios in Tuff 6, (2) decrease in Sr ratio in Tuff 8 at no significant change in Nd value, and (3) a shift to lower or higher Sr isotopic ratios in different layers of Tuff 7 without significant variations in Nd isotopic signature.

The $^{87}Sr/^{86}Sr$ value of 0.70451 obtained for Tuff 7 by Kasanzu et al. (2016) is similar to those measured in the white and gray tuffs. However, because the Nd isotopic composition of this sample is unknown, no direct comparison can be made with our data. Comparison of the new isotopic data for the Upper Laetolil tuffs with the data available for Sadiman, Mosonik and Essimingor show some similarities, as well as differences in their Sr and Nd isotopic compositions (Fig. 25), which will be discussed below.

6. Discussion

6.1. Source indicator minerals

Both previously published data (Hay, 1978, 1987; Barker and Milliken, 2008; McHenry, 2011; Zaitsev et al., 2015) and this work show that the Upper Laetolil marker tuffs are quite uniform in terms of their mineralogy. The assemblage of clinopyroxene, nepheline, garnet, perovskite, magnetite, apatite and titanite points to a magma of nephelinitic composition as the source of the Laetolil ash deposited between 3.85 and 3.63 Ma. Subsequently, ash beds were lithified into tuffs and underwent alteration (e.g., replacement of glass), but many of the primary minerals were either preserved intact or underwent limited alteration. Three mineralogical characteristics of the marker tuffs are particularly important for further discussion and will be considered in detail here: the absence of olivine, scarcity of alkali feldspar, and presence of melilite.

Olivine has never been reported in the Upper Laetoli tuffs, which effectively rules out primitive olivine-bearing nephelinitic magmas (e.g., Group II nephelinites and melanephelinites in the terminology of Le Bas, 1987) as the source of the UL tuffs. Alkali feldspar, interpreted to be sanidine on the basis of its optical properties, does occur in the Laetolil tuffs, but is uncommon. If this mineral were similar in abundance to nepheline and clinopyroxene, a phonolitic or phonotephritic magma source would have to be considered a likely source of the pyroclastic material at Laetoli. The Sadiman volcano contains several varieties of nephelinite, two of which contain abundant sanidine

Table 10

Composition of the silicate glass from melt inclusions (white and gray tuff layers of Tuff 7).

Host	clinopyroxene			garnet			magnetite		
	average (12)	min	max	average (8)	min	max	average (20)	min	max
SiO_2	38.12	36.03	41.67	44.85	44.16	45.61	35.06	30.16	42.38
TiO_2	1.68	1.38	1.97	0.36	0.25	0.48	1.69	1.13	2.80
Al_2O_3	10.73	8.60	13.55	11.09	10.83	11.39	10.95	9.73	12.15
Fe_2O_3	11.86	9.84	13.27	12.96	12.78	13.27	8.68	6.60	12.24
CaO	10.03	6.53	12.08	4.28	4.16	4.45	14.94	9.99	18.20
MgO	1.40	0.98	1.84	0.69	0.60	0.75	2.52	2.04	3.15
MnO	0.46	0.39	0.56	0.48	0.43	0.61	0.28	0.21	0.45
Na_2O	11.07	10.45	11.93	10.69	9.81	11.16	10.96	8.91	12.86
K_2O	5.58	4.65	6.04	7.13	7.02	7.26	3.79	3.19	5.11
SrO									0.71
P_2O_5	0.54	0.30	0.76	0.30	0.27	0.32	1.00	0.30	1.58
SO_3	0.92	0.72	1.15	0.90	0.67	1.05	0.81	0.40	1.50
Cl	0.35	0.28	0.43	0.26	0.23	0.30	0.37	0.17	0.51
-Cl,F=O	0.08			0.06			0.08		
Total	92.67			93.93			90.98		
(Na + K)/Al	2.26	1.92	2.76	2.28	2.14	2.41	2.02	1.70	2.38
Mg#	19.0	15.0	25.2	9.5	8.2	10.4	36.6	29.0	45.7

microphenocrysts. Phonolites with sanidine phenocrysts are also locally present as xenoliths in nephelinites (Zaitsev et al., 2011, 2012).

Melilite was first described from the marker tuffs at Laetoli by Hay (1978, p. 363) as "slightly to wholly altered to dense clay" and the bulk composition of Tuffs 1 and 6 (after calcite removal by acid leaching) was interpreted as melilititic. Melilite was also mentioned from ijolite blocks and "vitric particles" occurring in aeolian tuffs. Melilite in glass-rich aeolian tuffs is åkermanite, enriched in Mg (MgO = 8.0–9.8 wt%, Hay, 1978) compared with that from Tuff 7 (Table 3). Unfortunately, no compositional data on melilite from the marker tuffs was provided. On the basis of geological data, petrography, mineralogy and geochemistry, the air-fall (marker) tuffs were considered to be originally a mixture of melilititic and alkali-rich carbonatitic (natrocarbonatitic) ash, and Sadiman was proposed to be the source for these tuffs (Hay, 1978, 1986, 1987, Hay and Leaky, 1982; Hay and O'Neil, 1983). More recently, Peters et al. (2008, p. 51) described ash deposited at Laetoli as nephelinitic, noting also that "natrocarbonatitic ash was ejected in some eruptions".

Sadiman was termed a melilite nephelinite volcano by Barker and Milliken (2008), who referred to Hay (1987), Paslick et al. (1995),

Foster et al. (1997) and Wirth and Adelsberger (2002). In fact, Sadiman is not described as a melilite nephelinite volcano in any of these publications. Clasts of melilitite in Sadiman tuffs and agglomerates were mentioned by Dawson (2008), who cited geological map QDS 52 (Pickering, 1964) as his source. But, again, the description of Sadiman on that map does not contain any information about the presence of melilite-bearing rocks. Further, carbonatites have never been reported from Sadiman, and Barker and Milliken (2008) presented conclusive mineralogical evidence that the Footprint tuff from Locality 7 was not deposited as carbonatitic ash.

Despite all of these contradictions, Barker and Milliken (2008) are correct in their interpretation of the original ash composition deposited at Laetoli as crystal-vitric melilite nephelinite. Marker tuffs contain both crystal-bearing and crystal-free pellets and their proportions either for different tuffs or different layers within a single tuff are highly variable (Fig. 1). Layers of the laminated and Augite-biotite tuffs in Tuff 7 are examples of original ash with very high and very low volcanic glass content respectively (Figs. 6a and 7a).

Among marker tuffs melilite has been found as corroded crystals within pellets in the lower part of Tuff 7 only (white and gray tuffs)

Table 11

Composition of the carbonate globules from melt inclusions (white and gray tuff layers of Tuff 7).

| Host	magnetite														
Analysis	2	9	21	8	4	3	6	3	2	15	14	11	4	17	12
SiO_2	5.82	6.72	7.12	8.60	8.73	9.54	12.66	15.13	16.26	17.26	17.50	19.21	21.54	24.65	26.42
TiO_2	0.38	0.65	0.52	0.60	0.57	0.75	0.72	1.03	0.62	1.07	1.17	1.22	0.72	1.32	1.43
Al_2O_3	0.91	1.30	1.13	1.74	1.89	2.02	3.14	3.70	4.02	4.55	4.99	5.10	6.05	6.97	8.14
FeO	2.37	3.19	2.35	2.62	2.91	3.33	3.43	4.86	3.99	4.80	5.62	5.09	5.45	5.78	5.84
CaO	30.60	25.89	31.69	29.06	28.04	27.21	26.49	25.61	25.55	22.49	19.84	22.19	22.79	19.10	20.02
MgO	1.48	1.49	1.71	1.53	1.54	1.61	1.54	2.06	1.89	1.54	1.48	1.66	1.86	1.72	2.21
MnO	0.23												0.21	0.22	
Na_2O	9.44	15.27	7.98	7.04	9.71	7.47	7.47	9.33	12.19	6.50	10.64	6.69	9.17	7.63	6.56
K_2O	3.10	2.69	3.34	2.77	3.19	3.06	2.95	3.05	3.23	3.01	3.05	2.94	3.05	3.41	3.19
SrO	0.86	0.61	0.69	0.92	0.67	0.84	0.66	0.79	0.89	0.73		0.69			
BaO										0.41	0.41				
P_2O_5	4.15	3.19	4.26	3.92	3.41	3.41	3.53	2.91	3.25	2.96	1.81	3.19	3.02	2.31	1.76
SO_3	3.92	2.85	3.52	3.22	3.40	3.17	2.62	2.15	2.55	1.75	1.50	1.72	1.82	1.12	1.10
Cl	1.12	0.22	1.00	1.02	0.96	0.95	0.77	0.50	0.85	0.62	0.49	0.52	0.60	0.38	0.41
F	2.48	0.73	2.71	2.06	1.33	2.24	1.60		1.66	1.60	1.14	2.30	1.67	1.36	
-F,Cl=O	1.30	0.36	1.37	1.10	0.78	1.16	0.85	0.11	0.89	0.81	0.59	1.09	0.84	0.66	0.09
Total	65.56	64.44	66.65	64.00	65.57	64.44	66.73	71.01	76.06	68.48	69.05	71.43	77.11	75.31	76.99
(Na + K)/Al	20.8	21.6	14.8	8.38	10.3	7.72	4.93	5.04	5.86	3.07	4.17	2.78	3.04	2.33	1.75
Ca/(Na + K)	1.47	0.84	1.72	1.81	1.31	1.59	1.56	1.25	0.99	1.47	0.87	1.42	1.13	1.07	1.28
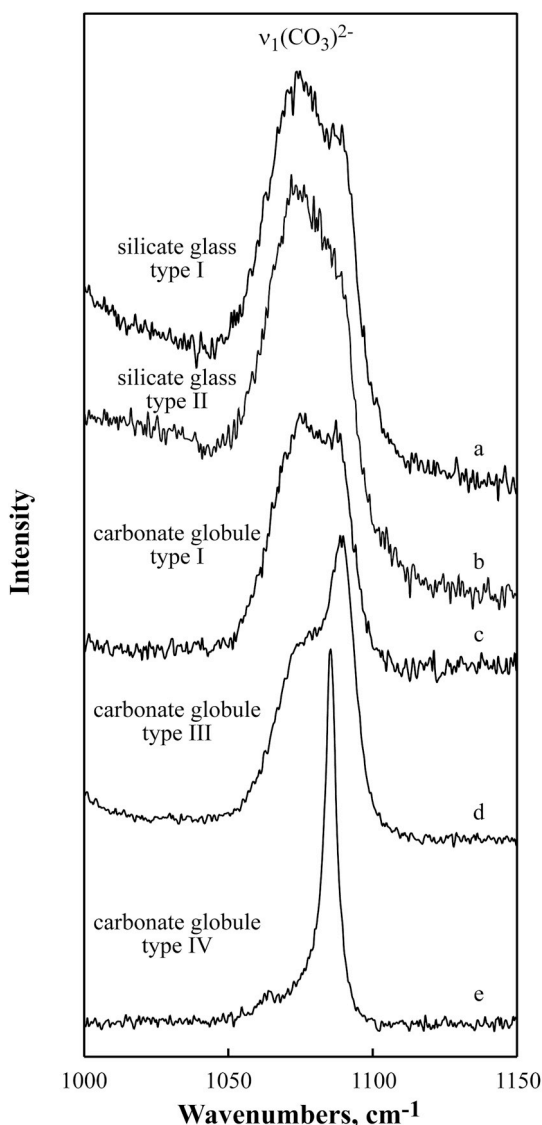
Fig. 24. Raman spectra of silicate glass and carbonate globules from melt inclusions.

(McHenry, 2011). Other marker tuffs as well as laminated and Augite-biotite tuffs from Tuff 7 contain tabular pseudomorphs which were interpreted by Hay (1978) as former melilite. The exception is Tuff 8 where both tabular and square-shaped (former nepheline) pseudomorphs were not observed during this study.

The composition of a melilite in both volcanic and plutonic rocks is variable and ranges from Na–Al-poor åkermanite to alumoåkermanite with a high Na and Al content (e.g. Egorov, 1969; Wiedenmann et al., 2009, 2010) and its composition can be used for volcanic source determination of remotely deposited ash layers (e.g. Balashova et al., 2018). In the case of melilite from Laetoli, its composition (Table 3) is similar to minerals from the Oldoinyo Lengai volcano (evolved melilite and combeite-wollastonite nephelinites, MgO = 0.6–2.0 wt%, Klaudius and Keller, 2006, Wiedenmann et al., 2009, 2010), Kerimasi (evolved melilite nephelinite, MgO = 3.5 wt%, this study), Mosonik (evolved melilite nephelinite, MgO = 2.1 wt%, this study) and Embagai (evolved nephelinite, MgO = 3.5 wt%, Mollel, 2007). Melilite is also mentioned from evolved tephri-phonolites and phonolite from the Essimingor volcano (MgO = 0.8–1.8 wt%) and one sample of primitive, high-Mg (MgO = 16.5 wt%) glassy picrite (Mana et al., 2012). Unfortunately, no melilite compositional data were reported.

Table 12
Rb–Sr and Sm–Nd isotope analytical data.

Tuff	Sample	Fraction	Rb ppm	Sr ppm	$^{87}Rb/^{86}Sr_m$	2σ	$^{87}Sr/^{86}Sr_m$	$^{87}Sr/^{86}Sr_i$	Sm ppm	Nd ppm	$^{147}Sm/^{144}Nd_m$	$^{143}Nd/^{144}Nd_m$	2σ	$^{143}Nd/^{144}Nd_i$
UL 8	LA 1.16	residual	73.34	124.5	1.7020	8	0.705439	0.705352	13.74	90.43	0.0918	0.512658	4	0.512656
		leached	7.702	956.3	0.0233	10	0.704636	0.704635	4.946	30.28	0.0988	0.512676	8	0.512674
	LA 10E.02	residual	103.4	189.2	1.5790	6	0.705509	0.705428	15.88	102.4	0.0938	0.512698	5	0.512696
		leached	20.71	2259	0.0265	22	0.704851	0.704850	11.90	65.47	0.1099	0.512718	4	0.512715
UL 7 Augite-biotite	LA 1.10	residual	19.25	181.8	0.3059	10	0.703669	0.703653	16.14	83.38	0.1171	0.512696	5	0.512693
		leached	21.63	1092	0.0572	6	0.704441	0.704438	2.821	16.07	0.1061	0.512725	5	0.512722
	LA 16.05	residual	26.03	166.5	0.4514	12	0.703667	0.703644	22.87	139.5	0.0991	0.512782	9	0.512780
		leached	17.52	1461	0.0347	4	0.704427	0.704425	3.685	21.65	0.1029	0.512739	8	0.512737
Laminated	NFP I/4	residual	17.78	166.3	0.3088	9	0.704460	0.704444	3.229	17.51	0.1115	0.512696	7	0.512693
		leached	6.009	2059	0.0084	13	0.704269	0.704269	11.51	47.11	0.1477	0.512693	3	0.512689
White	NFP I/4	residual	19.62	242	0.2343	16	0.704566	0.704554	6.556	38.04	0.1042	0.512712	4	0.512710
		leached	2.585	1497	0.0050	7	0.704420	0.704420	5.767	27.79	0.1255	0.512698	3	0.512695
Gray	NFP I/4	residual	13.62	173.8	0.2263	11	0.704550	0.704538	2.054	11.17	0.1112	0.512693	4	0.512690
		leached	2.648	1687	0.0045	9	0.705047	0.705047	7.429	35.18	0.1277	0.512697	4	0.512694
UL 6	LA 1.06	residual	64.41	150.7	1.2346	8	0.704374	0.704311	6.472	27.16	0.1441	0.512591	4	0.512588
		leached	11.22	2046	0.0158	17	0.704348	0.704347	5.033	29.91	0.1018	0.512505	9	0.512503

m – measured, i – initial (calculated for 3.66 Ma).
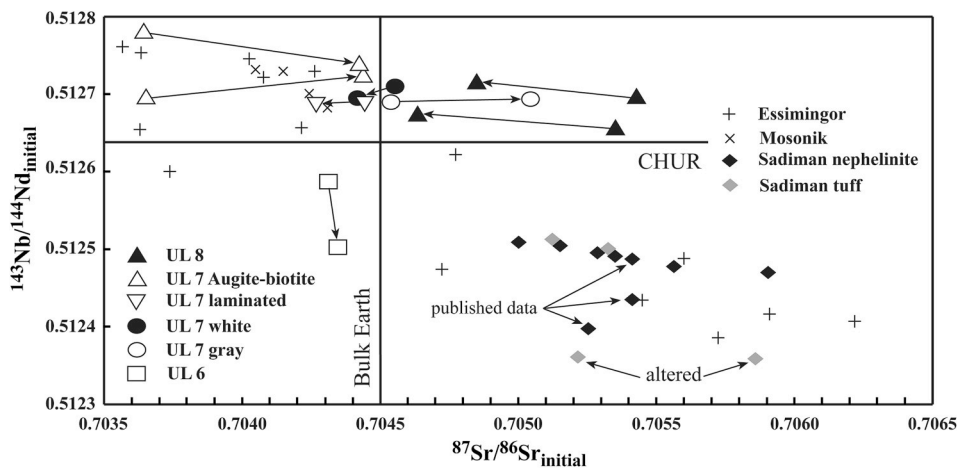
6.2. Melt inclusions and source composition

Additional important information concerning the source of the Upper Laetolil marker tuffs is presented by melt inclusions in the primary silicate and oxide minerals. Data from Zaitsev et al. (2015) and this, more detailed, study show the presence of two inclusion types, one consisting of silicate glass only and another composed of silicate glass and carbonate globules.

The silicate glass is peralkaline with a (Na + K)/Al ratio of 1.7–2.8 (Na_2O = 8.9–12.9 wt%, K_2O = 3.2–7.3 wt%) and a low silica content (SiO_2 = 30.2–45.6 wt%). Other major elements (Al, Fe, Ca) and minor Mg show significant variations in abundance, and inclusions hosted by different minerals contain glass of different composition (Table 10). Low analytical totals and Raman spectroscopy strongly suggest the presence of $(CO_3)^{2-}$ in the glass (Fig. 23; Morizet et al., 2013, 2014). Carbonate content in silicate glasses from melt inclusions in minerals from Oldoinyo Lengai (up to 9 wt% CO_2: Maarten de Moor et al., 2013) and experimental data show high solubility of CO_2 in alkali-rich silicate glasses (up to 15 wt%: Morizet et al., 2013). We are not, however, certain at this point whether the carbonate component is present within the studied melt inclusions as carbonate anions dissolved in glass, or as microemulsion of carbonate globules.

Carbonate globules coexisting with silicate glass are rich in Ca (up to 31.7 wt% CaO), with elevated alkali (9.5–19.6 wt% Na_2O + K_2O) and variable SiO_2 (5.8–26.4 wt% SiO_2) contents (Table 11). The latter is dependent on the size of carbonate globules and, at least in some cases, high SiO_2 values could be an artefact resulting from excitation of the host glass during the EDS analysis. An alternative explanation is that separation of carbonate and silicate melts was not complete (Zaitsev et al., 2015). Compositionally, the carbonate component can be interpreted as "calciocarbonatite"; the globules have a much higher Ca/(Na + K) ratio (0.8–1.8, averaging 1.3), relative to "natrocarbonatite" globules in melt inclusions at Oldoinyo Lengai (0.1–0.5, averaging 0.2: Mitchell, 2009, Mitchell and Dawson, 2012). The globules analysed in the present study are closer in composition to carbonate phases hosted by melt inclusions in minerals from Kerimasi carbonatites [Ca/(Na + K) = 0.5–3.5, averaging 1.7] and silicate rocks (1.3–2.1 and 1.7, respectively: Guzmics et al., 2011, 2012). Kerimasi is a young extinct volcano, located near Oldoinyo Lengai (see Section 1), and contains both volcanic and plutonic carbonatites (Hay, 1983; Mariano and Roeder, 1983; Church, 1995; Reguir et al., 2008; Zaitsev, 2010; Zaitsev et al., 2010, 2011; Guzmics et al., 2011). The latter are typical calcite carbonatites, whereas the former contain primary calcite and calcite pseudomorphs after nyerereite.

Raman spectra of SiO_2-rich (11–15 wt%) and SiO_2-poor (6–8.5 wt%) carbonate globules show clear differences (Fig. 23). The spectra of SiO_2-rich globules contain broad bands composed of either two peaks or one

peak and a shoulder, and are similar to those obtained from silicate glasses (Fig. 24). These spectral features may indicate the presence of Na–Ca carbonates (Golovin et al., 2015, 2017; Sekisova et al., 2015). In contrast, SiO_2-poor globules give a single symmetrical peak at 1085 cm^{-1} (Fig. 23), which points to their calcitic composition.

6.3. Compositional heterogeneity of primary minerals

The Upper Laetolil tuffs cover a large area, and marker tuffs are observed at numerous localities and different elevations (Fig. 1). The tuffs were obviously affected by weathering to a different extent and locally disintegrated. The best example of this is the stratigraphy of Tuff 7 at Sites G and S of Locality 8 (Table 2, Figs. 4 and 5). Site S lacks the upper part of the Augite-biotite tuff, which is observed at site G (about 130 m to the north) as a conspicuous layer some 22–23 cm in thickness. The nature of contact between the white and gray tuffs at Site S (Fig. 11) suggests partial disintegration of the latter before the deposition of a new ash bed (presently, the white tuff). These features complicate precise identification of individual markers during field studies and their correlation among different localities. However, both these tasks are quite important for palaeo-anthropological studies at Laetoli because hominin remains and footprints must be accurately positioned in the stratigraphic record (e.g., Harrison, 2011a, 2011b; Masao et al., 2016).

The composition of primary minerals, particularly variations in major- and minor-element abundances, are important for tephrostratigraphic reconstructions. Selected primary minerals from the Lower and Upper Laetolil tuffs, as well as the younger Ndolanya and Naibadad tuffs, were studied by McHenry (2011), and the compositions of clinopyroxene, garnet, perovskite, magnetite and titanite were used to distinguish different tuff units. There are two major problems, however, with these data. First, some analyses have low totals even though none of the examined minerals contain any appreciable H_2O. Secondly, there are no values reported for concentrations of key minor elements substituting in the structure of these minerals (e.g., Sr in melilite, Zr and Nb in garnet, REE, Nb and Sr in perovskite, V in magnetite). Therefore, all common primary minerals (nepheline, garnet, perovskite and magnetite) and accessory sanidine were re-analyzed during this study to produce a representative set of key minor- and trace-element data.

The marker tuffs are highly altered rocks (Hay, 1978, 1987, Barker and Milliken, 2008), in which all volcanic glass and some primary minerals were fully or partially replaced by secondary montmorillonite, phillipsite and calcite (Figs. 2, 6–10, 12, 13). Ash/tuff alteration could also have had an effect on the composition of minerals, which is clearly observed for nepheline. Its compositions (Fig. 15) suggest low crystallization temperature (< 500 °C), which is unrealistic for nephelinitic magmas (e.g., Kjarsgaard, 1998). Another noteworthy feature of the

nepheline is its high Ca content (0.4–1.7 wt% CaO at an average value of 1.0 wt%); only two grains have much lower levels of this element (< 0.2 wt% CaO). Fresh, unaltered nephelinites from Sadiman and Mosonik contain nepheline with CaO contents < 0.5 wt% (Paslick et al., 1996; Zaitsev et al., 2012, Zaitsev et al. unpubl. data), whereasnepheline from highly altered rocks contains up to 1.5 wt% CaO. We interpret this as evidence of nepheline re-equilibration with Ca-rich fluids during the post-depositional lithification of Laetoli tephras.

Garnet, perovskite and magnetite do not show any evidence of chemical changes due to alteration (Tables 5–7, Figs. 6a and 9a,b, 10d), and the latter two minerals have been previously suggested as suitable tephrostratigraphic indicators for the Upper Laetolil marker tuffs: "Titanomagnetite and perovskite compositions help distinguish individual Upper Laetolil tuffs, and divide the bed compositionally into lower (UL 1–4) and upper (UL 5–8) units" (McHenry, 2011, p. 121). This suggestion, however, is not supported by the new analytical data, which include minor elements overlooked in the previous work. All three aforementioned minerals are characterized by wide variations in composition, so much so in fact that their major and minor element distributions overlap across the different marker tuffs examined here (Figs. 16–18).

Garnet in the UL marker tuffs forms a continuous solid solution between Ti-poor (0.8 wt% TiO_2), essentially pure andradite (96 mol.%) to schorlomite (18.9 wt% TiO_2) containing merely 19 mol.% andradite. The recorded variations, particularly in Tuff 1 (Fig. 16), are not related to chemical variations within a single crystal, although core-rim zonation is observed in some grains; instead, the tuffs contain crystals of quite variable compositions. Two or three compositional varieties of garnet are present in each marker tuff.

Individual marker units cannot be distinguished on the basis of perovskite compositions either. Tuffs 2 and 6 contain perovskite with small variations in the content of major and minor elements, possibly representing a single population of crystals. Other marker tuffs, particularly Tuffs 7 and 8, contain compositionally heterogeneous perovskite crystals (Fig. 17). Perovskite from the Sadiman nephelinites (Zaitsev et al., 2012) is slightly enriched in light REE in comparison with perovskite from Tuffs 1 to 7 (white and gray tuffs only) and is similar in its minor-element distributions to perovskite from the Augite-biotite tuff of Tuff 7 and from Tuff 8 (Fig. 17). Nephelinites from Mosonik contain perovskite with a Nb content similar to that in the marker tuffs, but appreciably higher levels of light REE (3.1–6.5 wt% REE_2O_3, Paslick et al., 1996).

Finally, the data available for magnetite (Fig. 18) provide further strong evidence for high heterogeneity of the Upper Laetolil tuffs. The marker tuffs contain several populations of magnetite, which are quite different from one another in composition, particularly in terms of their Mg and Al contents. These vary from Mg–Al-poor, Ti-bearing magnetite (0.1 wt% MgO and Al_2O_3; 8.6 wt% TiO_2) to a Mg–Al–Ti-rich varieties (up to 3.7 wt% Al_2O_3, 7.5 wt% MgO and 14.6 wt% TiO_2). While Laetoli magnetite with low Mg and Al contents (< 1.5 wt% respective oxides) is similar to magnetite from the Sadiman and Mosonik nephelinites (Paslick et al., 1996; Zaitsev et al., 2012, 2015), the Mg- and Al-rich varieties have no documented analogues in these rocks.

Magnetite is a common mineral in volcanic and plutonic silicate rocks, as well as in carbonatites throughout the Crater Highlands and Gregory Rift. However, only a small number of published magnetite analyses approach the levels of Mg, Al and Ti enrichment documented in some grains from the marker tuffs. These include data for basanites from Ngorongoro, Gelai and Ketumbeine, and foidite from the so-called "Older Extrusives" (Paslick et al., 1996). Magnetite and related minerals from the Kerimasi and Oldoinyo Lengai volcanoes are much better studied (Reguir et al., 2008; Guzmics et al., 2011; Zaitsev et al., 2013; Mattsson et al., 2018), but are characterized by strong enrichment in Mg (Kerimasi) or Mn (Oldoinyo Lengai). Mollel (2007) has investigated magnetite from Ogol, Lemagurut, Olmoti, Embagai and Oldeani, but only basalt and trachyandesite samples from the latter

contain magnetite approaching the Laetoli material in composition. More importantly, some of his data show elevated levels of elements that cannot substitute in this mineral to any significant extent, like P_2O_5 (up to 0.8 wt%), Na_2O (up to 0.2 wt%) and F (up to 0.2 wt%). These anomalous values raise questions regarding the homogeneity of analyzed areas and validity of the analytical protocol.

The mineralogical evidence discussed above suggests that the Upper Laetolil marker tuffs contain several populations of minerals, which probably crystallized from different melt batches of differing composition. We suggest that during the eruption of a source volcano, gas-magma mixtures disrupted earlier-solidified rocks (probably, both plutonic and volcanic) and became contaminated with crystals from different rock types. The disrupted rocks could be either consanguineous cumulate rocks, shallow intrusions, lavas, or even buried older extrusive series similar to those exposed in the Gregory Rift escarpment (Neukirchen et al., 2010).

6.4. Trace elements variability

Severe alteration of the Upper Laetolil marker tuffs implies that their composition differs from that of the freshly deposited ash. One should expect that certain major, minor and trace elements were mobile during the cementation and alteration of the ash. A study of volcanic tuffs from Olduvai Gorge by McHenry (2009, 2010) has shown that some elements could be mobile during their low-temperature alteration, but in general, the assemblage of authigenic smectite and zeolite minerals (montmorillonite + phillipsite in our samples) retained the composition of precursor volcanic tephra.

In terms of their chemical composition, the Laetolil tuffs are an H_2O-rich silicate-carbonate rock (Table 9, Fig. 20) with highly variable proportions of secondary calcite, montmorillonite, phillipsite, primary silicate (clinopyroxene, garnet, nepheline, etc.) and oxide phases (magnetite, perovskite). Despite this diversity, the multi-element normalized profiles and REE distributions pf the UL tuffs (Figs. 21–22) are strikingly similar and support a nephelinitic magma source.

For continuous lateral correlation of the marker tuffs, more data are required. Our detailed study of the vertical cross-sections of Tuff 7, including Site S with recently discovered *Australopithecus afarensis* footprints, provide information about the relations among its different constituent units. Field observations and mineralogical studies show that ash deposition occurred during four major eruptive events, which ultimately produced the gray, white, laminated and Augite-biotite layers within Tuff 7. The observed variations in major- and trace-element distributions, including petrogenetic element ratios (e.g., Th/U, Ce/Pb), allow the examined rocks to be grouped as follows: (1) gray and white tuffs, (2) laminated tuff and (3) Augite-biotite tuff.

The gray and white tuffs are almost identical in composition and differ significantly from the Augite-biotite tuff. Specifically, the latter is strongly enriched in SiO_2, TiO_2, Al_2O_3, FeO, MgO, Zr, Nb, REE and Th when compared with the white or gray tuffs, which in their turn show high levels of CaO, CO_2 and Sr (Table 9). Element ratios also differ between the two rock groups, i.e. the Th/U and Ce/Pb values are much higher in the Augite-biotite unit (2.6–3.9 and 39–105, respectively) relative to the gray and white tuffs (0.2–0.6 and 10–22, respectively), whereas the Nb/Ta ratio shows the opposite relationship (12–31 vs. 43–94, respectively). The laminated tuff shows compositional similarities and differences when compared to the Augite-biotite and gray + white tuffs. Some element abundances and element ratios in the laminated tuff are similar to those in the Augite-biotite tuff (e.g., SiO_2, Al_2O_3, Na_2O, Zr, Nb), whereas being closer to the gray and white tuffs in some of their other geochemical characteristics (e.g., Sr, Th/U, Nb/Ta values). At the same time, the laminated tuff differs from the other two groups in being enriched in H_2O, P_2O_5, Cu, Pb and U (Table 9).

6.5. Heterogeneity of Sr–Nd isotopic composition

The observed geochemical variations among the different constituent units of Tuff 7 are further supported by the Sr and Nd isotopic data (Table 12, Fig. 25). Residual fractions from the gray and white tuffs are nearly identical in terms of their initial $^{87}Sr/^{86}Sr$ and $^{144}Nd/^{143}Nd$ ratios (0.70455–0.70457 and 0.51269–0.51271, respectively), whereas the residual fraction from the laminated tuff has the same Nd isotopic ratio (0.51270), but slightly lower Sr isotopic ratio (0.70446). The insoluble residuum from the Augite-biotite unit is characterized by the lowest $^{87}Sr/^{86}Sr$ ratio (0.70367) of all the studied samples, but yielded $^{144}Nd/^{143}Nd$ ratios that are slightly higher compared to those for the gray, white and laminated tuffs.

Tuffs 6 and 8, which lie below and above Tuff 7, respectively, are characterized by quite different isotopic values (Table 12, Fig. 25). The residual fraction from Tuff 6 gave the lowest $^{144}Nd/^{143}Nd$ ratio (0.51259) among all tuff samples examined in the present study, and its $^{87}Sr/^{86}Sr$ ratio (0.70437) is slightly lower compared to the gray, white and laminated tuffs. The insoluble residuum from Tuff 8 is distinct in its high $^{87}Sr/^{86}Sr$ ratio (0.70544–0.70551), which greatly exceeds those measured in the rest of our samples.

The documented variations in Sr and Nd isotopic data suggest extreme heterogeneity of volcanic source(s) that produced the Laetolil tuffs. When compared with isotopic data available for volcanoes of similar age (Fig. 25), it is quite clear that the UL tuffs are distinct from the Sadiman nephelinitic lavas and tuffs. The latter form a linear trend within the "enriched mantle" quadrant, and approach the isotopic compositions of evolved low-Mg rock from Essimingor. Tuff 7 and, in part, Tuff 6 are close in isotopic composition to primitive high-Mg lavas from Essimingor and also to primitive basanite and evolved nephelinites from Mosonik. Tuff 6 differs in isotopic composition from all three volcanoes (Fig. 25).

The large variations in Sr and Nd data among the Essimingor lavas were explained by the involvement of two isotopic reservoirs, one of which is a depleted mantle component and another is a crustal component with high Sr and low Nd isotopic ratios (Mana et al., 2012). Primitive lavas with low Sr, high Nd isotopic ratios and high Ce/Pb values were not affected by crustal assimilation, whereas more evolved lavas, characterized by high Sr, low Nd isotopic ratios and low Ce/Pb ratios, were contaminated, possibly by granitic material from the continental crust. It is interesting that the Mosonik volcano, which also contains both primitive and evolved rocks with quite different Ce/Pb ratios (ranging from 25.6 in basanite to 9.7–16.5 in nephelinite), is characterized by similar Sr and Nd isotopic ratios and low $^{87}Sr/^{86}Sr$ values (0.70405–0.70425; Paslick et al., 1996).

Leached fractions from Tuffs 6, 7 and 8 are also heterogeneous; their initial $^{87}Sr/^{86}Sr$ and $^{144}Nd/^{143}Nd$ ratios exhibit large variations. We assume that the Sr and Nd isotopic compositions of these samples derived from two sources: a juvenile source, represented by freshly deposited ash (including Sr and Nd substituting in primary minerals and released from volcanic glass during its alteration) and a secondary source, represented by surface and meteoric water. Within Tuff 7, leached fractions from the white, laminated and Augite-biotite tuffs are similar in isotopic composition; their initial $^{87}Sr/^{86}Sr$ and $^{144}Nd/^{143}Nd$ values are 0.70427–0.70444 and 0.51269–0.51274, respectively. The leached fraction from the gray tuff has a similar Nd ratio (0.51269), but its $^{87}Sr/^{86}Sr$ value is significantly higher (0.70505). The leachate from Tuff 8 gave a similar range of Nd isotopic ratios (051268–0.51272), and Sr ratios intermediate with respect to those in the white, laminated and Augite-biotite tuffs on the one hand and gray tuff on the other (0.70464–0.70485). The leachate from Tuff 6 is quite unlike the rest of the studied material; in contrast to the latter, the leached and residual fractions have similar Sr isotopic budgets, differ significantly in Nd composition. The leached fraction has the lowest $^{144}Nd/^{143}Nd$ ratio of all the analyzed samples (0.51250). Similar variations are observed at Sadiman, i.e. highly altered kaolinite-bearing tuffs and fresh

nephelinite lavas and tuffs exhibit similar Sr isotopic signatures, but the latter have less radiogenic Nd compositions (Fig. 25).

The Sr and Nd concentrations in groundwater 3.66 Ma ago are not known, but the present day water, collected in 2016 from black sand covering the white tuff with *Australopithecus afarensis* footprints, contains just 2.1 ppm Sr (Zaitsev et al., 2017). Such low levels imply that surface water would have had very little effect on the isotopic composition of precipitating secondary minerals, unless a large amount of mineral(s) with quite a different $^{87}Sr/^{86}Sr$ ratio (e.g., feldspars from crustal rocks) were dissolved by these fluids. This scenario could explain why the Sr isotopic composition of the soluble fraction from the gray and Augite-biotite tuffs is shifted toward more radiogenic values. Another possible explanation is that precursor ash was heterogeneous in terms of its Sr and Nd isotopic composition due to the presence of minerals and glass of different isotopic composition. Such heterogeneity has been documented, for example, for nephelinites from the Napak volcano (Uganda), where clinopyroxene phenocrysts and their host lava are not in isotopic equilibrium (Simonetti and Bell, 1993). Compositionally different mineral populations in the Laetolil marker tuffs (see above) could derive from magma batches of different isotopic composition, which would explain at least some of the observed variations.

7. Conclusions

The Upper Laetolil marker tuffs are mineralogically similar rocks that contain the same mineral assemblages of primary and secondary minerals. Their mineralogical similarity suggests a single volcanic source or, possibly, several sources with similar magma compositions. Only ash that produced Tuff 8 could have derived from a slightly different source because it does not contain any obvious pseudomorphs after melilite and nepheline, at least in the samples examined in the present work.

On the basis of mineralogical and geochemical data presented here, and published work (Hay, 1978, 1987; Barker and Milliken, 2008; McHenry, 2011; Zaitsev et al., 2011, 2015), we conclude that the Upper Laetolil tuffs originally represented crystal or vitric ash of evolved melilite-nephelinitic composition, and not a melilitite-(natro)carbonatite. However, the occurrence of alkaline carbonate-bearing silicate melt inclusions in primary magnetite, clinopyroxene and garnet supports R. Hay's conclusion that the ash could have erupted from a volcanic source that also produced carbonatites.

Despite their mineralogical similarities, the marker tuffs show heterogeneity in terms of their texture, structure, proportion of crystal-free and crystal-bearing pellets, volume of cement and degree of low-temperature alteration. Given great variations in the proportion of primary minerals, the absence of fresh volcanic glass and abundance of calcite in the cement, the Laetolil rocks are best described as crystal or vitric ash replaced by montmorillonite ("palagonitized" *sensu lato*) and subsequently cemented by calcite. Any of the marker tuffs could be termed palagonitized tuff with a secondary calcitic cement.

Primary minerals in the marker tuffs are characterized by wide compositional variations; two or more mineral populations are present within each marker tuff. This suggests that these units consist of minerals formed at different stages in the evolution of their parental volcanic source and derived from compositionally different magma batches. Correlation of tuff horizons between different localities exclusively on the basis of their mineral composition is not possible given the observed variations. At present, none of the studied minerals can be confidently used as a tephrochronological indicator, at least within the Laetoli sequence.

The marker tuffs are also indistinguishable in their bulk chemical composition; only the white and gray layers within Tuff 7 can be identified using the major-element geochemsitry, (e.g., SiO_2, Al_2O_3, CaO and CO_2 contents). Tuff 7 is the best studied marker tuff at Laetoli, particularly at Sites G and S of Locality 8. Its scientific importance owes to the presence of hominin footprints left by *Australopithecus afarensis*

(Masao et al., 2016) and to the plans of the Ngorongoro Conservation Area Authority of Tanzania to establish a Laetoli Footprints Museum (Zaitsev et al., 2016, 2017).

The available data (field observations, stratigraphy, mineralogy and geochemistry) show that Tuff 7 is very heterogeneous, both vertically and laterally. Summarizing the data presented above, we suggest the following scenario of tuff formation involving four major events:

(1) Deposition of fine-to coarse-grained vitric ash with a small proportion of primary crystals (at present, the well-stratified gray tuff layer); strong erosion of the ash surface in some areas;
(2) Deposition of medium-to coarse-grained vitric ash with a small proportion of primary crystals (at present, the unstratified white tuff layer);
(3) Deposition of fine-to medium-grained vitric ash (at present, the well-stratified laminated tuff layer);
(4) Deposition of medium-to coarse-grained crystal ash (at present, the crudely stratified Augite-biotite tuff); weathering and erosion of this unit in some areas.

The available mineralogical, major- and trace-element geochemical and Sr–Nd isotopic data suggest that the crystal-bearing vitric ash deposited during stages (1) and (2) was indistinguishable in composition and highly likely originated from the same volcanic source, but with a hiatus between the eruptions. Both tuffs show similar element distributions, as well as comparable element and isotopic ratios.

The tephra deposited at stage (3) was probably also derived from the same source, as indicated by its Sr and Nd isotopic composition. However, the ash was predominantly vitric and contained relatively few crystals of primary minerals. A distinct volcanic source should be considered for the final stage of Tuff 7 deposition. This is suggested by the mineralogical characteristics, trace-element geochemistry and Sr–Nd isotopic composition of the residual fraction from this unit. It does not mean, however, that the source of the Augite-biotite crystal ash was another volcanic vent. It is possible that this material derived from a compositionally different gas-magma mixture compared to the previous three eruptions.

The significantly different initial Sr and Nd ratios measured for Tuffs 6 and 8 indicate that their formation also involved compositionally distinct volcanic sources. Finally, Sr and Nd isotopic data for Tuffs 6, 7 and 8 show that the Sadiman volcano is an unlikely source for these three marker units at Laetoli. Previously, this was suggested on the basis of mineralogical data (Zaitsev et al., 2011, 2015), but Sadiman is still being referred to as the most likely source for the Laetolil tuffs and particularly for the Footprint tuff (Mollel, Swisher III, 2012; Su, Harrison, 2015; Kasanzu et al., 2016), largely because of its age and proximity.

At present, only two volcanoes with similar ages and/or mineralogy to the Laetolil tuffs are mineralogically and geochemically comparable with the Upper Laetolil marker tuffs, namely Essimingor and Mosonik. However, both are located far from Laetoli (about 100 to east for Essimingor and a similar distance, but north-east for Mosonik) and it remains to be determined whether such considerable quantities of ash, including coarse-grained material, could be transported over such long distances.

Acknowledgements

Appendix A. Supplementary data

Supplementary data to this article can be found online at https://doi.org/10.1016/j.jafrearsci.2019.103561.

References

Bagdasaryan, G.P., Gerasimovskiy, V.I., Polyakov, A.I., Gukasyan, R.K., 1973. Age of volcanic rocks in the rift zones of East Africa. Geochem. Int. 10, 66–71.

Balashova, A., Mattsson, H.B., Hirt, A.M., 2018. New tephrostratigraphic data from Lake Emakat (northern Tanzania): implications for the eruptive history of the Oldoinyo Lengai volcano. J. Afr. Earth Sci. 147, 374–382.

Barker, D.D., Milliken, K.L., 2008. Cementation of the footprint tuff, Laetoli, Tanzania. Can. Mineral. 46, 831–841.

Campbell, L.S., Dyer, A., Williams, C., Lythgoe, P.R., 2012. The masquerade of alkaline–carbonatitic tuffs by zeolites: a new global pathfinder hypothesis. Miner. Depos. 47, 371–382.

Chaudhuri, S., Brookins, D.G., 1979. The Rb-Sr systematics and acid-leached clay minerals. Chem. Geol. 231–242 1979.

Church, A.A., 1995. The Petrology of the Kerimasi Carbonatite Volcano and the Carbonatites of Oldoinyo Lengai with a Review of Other Occurrences of Extrusive Carbonatites. PhD Thesis. University of London, London, pp. 384.

Curtis, G.H., Hay, R.L., 1972. Further geological studies and potassium-argon dating at Olduvai Gorge and Ngorongoro crater. In: Bishop, W.W., Miller, J.A. (Eds.), Calibration of Hominoid Evolution. Scottish Academic, Edinburgh, pp. 289–301.

Dawson, J.B., 2008. The Gregory Rift Valley and Neogene-Revent Volcanoes of Northern Tanzania. Geological Society, London Geological Society Memoir No. 33.

de Moor, J.M., Fischer, T.P., King, P.L., Botcharnikov, R.E., Hervig, R., Hilton, D.R., Barry, P.H., Mangasini, F., Ramirez, C., 2013. Volatile-rich silicate melts from Oldoinyo Lengai volcano (Tanzania): implications for carbonatite genesis and eruptive behavior. J. Earth Planet. Sc. Lett. 361, 379–390.

Deino, A.L., 2011. $^{40}Ar/^{39}Ar$ dating of Laetoli, Tanzania. In: Harrison, T. (Ed.), Paleontology and Geology of Laetoli: Human Evolution in Context. Volume 1: Geology, Geochronology, Paleoecology and Paleoenvironment. Springer, Dordrecht, pp. 77–97.

Ditchfield, P., Harrison, T., 2011. Sedimentology, lithostratigraphy and depositional history of the Laetoli area. In: Harrison, T. (Ed.), Paleontology and Geology of Laetoli: Human Evolution in Context. Volume 1: Geology, Geochronology, Paleoecology and Paleoenvironment. Springer, Dordrecht, pp. 47–76.

Drake, R., Curtis, G.H., 1987. K-Ar geochronology of the Laetoli fossil localities. In: Leakey, M.D., Harris, J.M. (Eds.), Laetoli: a Pliocene Site in Northern Tanzania. Clarendon Press, Oxford, pp. 48–52.

Egorov, L.S., 1969. Melilitic Rocks of Maimecha-Kotuy Province. Nedra, Leningrad, pp. 247 (in Russian).

Evans, A.L., Fairhead, J.D., Mitchell, J.G., 1971. Potassium–argon ages from the volcanic province of northern Tanzania. Nature 229, 19–20.

Ferrat, M., Weiss, D.J., Strekopytov, S., 2012. A single procedure for the accurate and precise quantification of the rare earth elements, Sc, Y, Th and Pb in dust and peat for provenance tracing in climate and environmental studies. Talanta 93, 415–423.

Foster, A., Ebinger, C., Mbede, E., Rex, D., 1997. Tectonic development of the northern Tanzanian sector of the east African rift system. J. Geol. Soc., London 154, 689–700.

Frank-Kamenetsky, V.A. (Ed.), 1975. Instructions to the X-Ray Investigation of Minerals. Nedra, Leningrad, pp. 397 (in Russian).

Frank-Kamenetsky, V.A. (Ed.), 1983. X-ray Analysis of Most Importnat Types of Rock-Forming Minerals (Layer and Framework Silicates). Nedra, Leningrad, pp. 359 (In

Russian).

Golovin, A.V., Korsakov, A.V., Zaitsev, A.N., 2015. *In situ* ambient and high-temperature Raman spectroscopic studies of nyerereite $(Na,K)_2Ca(CO_3)_2$: can hexagonal zemkorite be stable at earth-surface conditions? J. Raman Spectrosc. 46, 904–912.

Golovin, A.V., Korsakov, A.V., Gavryushkin, P.N., Zaitsev, A.N., Thomas, V.G., Moine, B.N., 2017. Raman spectra of nyerereite, gregoryite, and synthetic pure $Na_2Ca(CO_3)_2$: diversity and application for the study micro inclusions. J. Raman Spectrosc. 48, 1559–1565.

Guzmics, T., Mitchell, R.H., Szabó, C., Berkesi, M., Milke, R., Abart, R., 2011. Carbonatite melt inclusions in coexisting magnetite, apatite and monticellite in Kerimasi calcio-carbonatite, Tanzania: melt evolution and petrogenesis. Contrib. Mineral. Petrol. 161, 177–196.

Guzmics, T., Mitchell, R.H., Szabó, C., Berkesi, M., Milke, R., Batter, K., 2012. Liquid immiscibility between silicate, carbonate and sulfide melts inclusions hosted in co-precipitated minerals from Kerimasi volcano (Tanzania): evolution of carbonated nephelinitic magma. Contrib. Mineral. Petrol. 164, 101–122.

Hamilton, D.L., 1961. Nephelines as crystallisation temperature indicators. J. Geol. 69, 321–329.

Paleontology and geology of Laetoli: human evolution in Context. In: In: Harrison, T. (Ed.), Geology, Geochronology, Paleoecology and Paleoenvironment 1. Springer, Dordrecht, pp. 401.

Paleontology and geology of Laetoli: human evolution in Context. In: In: Harrison, T. (Ed.), Fossil Hominins and the Associated Fauna 2. Springer, Dordrecht, pp. 600.

Hay, R.L., 1978. Melilitite-carbonatite tuffs in the Laetoli beds of Tanzania. Contrib. Mineral. Petrol. 67, 357–367.

Hay, R.L., 1983. Natrocarbonatite tephra of Kerimasi volcano, Tanzania. Geology 11, 599–602.

Hay, R.L., 1986. Role of tephra in the preservation of fossils in Cenozoic deposits in East Africa. In: Sedimentation in the African Rifts, vol. 25. Geological Society Special Publications, pp. 339–344.

Hay, R.L., 1987. Geology of the Laetoli area. In: Leakey, M.D., Harris, J.M. (Eds.), Laetoli, a Pliocene Site in Northern Tanzania. Clarendon Press, Oxford, pp. 23–47.

Hay, R.L., Leaky, M.D., 1982. The fossil footprints of Laetoli. Sci. Am. 246 (2), 50–57.

Hay, R., O'Neil, J.R., 1983. Carbonatite tufts in the Laetolil beds of Tanzania and the Kaiserstuhl in Germany. Contrib. Mineral. Petrol. 82, 403–406.

Isaac, G.L., Curtis, G.H., 1974. Age of early Acheulian industries from the Peninj group, Tanzania. Nature 249, 624–627.

Kasanzu, C.H., Maboko, M.A.H., Manya, S., 2016. Reconstruction of Pliocene-Pleistocene sediment sources and weathering intensity in the paleo-life rich Olduvai and Laetoli basins of northern Tanzania using major and trace element geochemistry and Sr isotopic data. J. Afr. Earth Sci. 123, 89–98.

Kjarsgaard, B.A., 1998. Phase relations of a carbonated high-CaO nephelinite at 0.2 and 0.5 GPa. J. Petrol. 39, 2061–2075.

Klaudius, J., Keller, J., 2006. Peralkaline silicate lavas at Oldoinyo Lengai, Tanzania. Lithos 91, 173–190.

Le Bas, M.J., 1987. Nephelinites and carbonatites. Geol. Soc. Lond. Spec. Publ. 30, 53–83.

Leakey, M.D., Hay, R.L., 1979. Pliocene footprints in the Laetolil beds at Laetoli, northern Tanzania. Nature 278, 317–323.

Mana, S., Furman, T., Carr, M.J., Mollel, G.F., Mortlock, R.A., Feigenson, M.D., Turrin, B.D., Swisher III, C.C., 2012. Geochronology and geochemistry of the Essimingor volcano: melting of metasomatized lithospheric mantle beneath the North Tanzanian Divergence zone (East African Rift). Lithos 155, 310–325.

Mana, S., Furman, T., Turrin, B.D., Feigenson, M.D., Swisher III, C.C., 2015. Magmatic activity across the east African north tanzanian divergence zone. J. Geol. Soc. 172, 368–389.

Manega, P.C., 1993. Geochronology, Geochemistry and Isotopic Study of the Plio-Pleistocene Hominid Sites and the Ngorongoro Volcanic Highland in Northern Tanzania (Ph.D. thesis). University of Colorado, USA.

Mariano, A.N., Roeder, P.L., 1983. Kerimasi: a neglected carbonatite volcano. J. Geol. 91, 449–455.

Masao, F.N., Ichumbaki, E.B., Cherin, M., Barili, A., Boschian, G., Iurino, D.A., Menconero, S., Moggi-Cecchi, J., Manzi, G., 2016. New footprints from Laetoli (Tanzania) provide evidence for marked body size variation in early hominins. eLife 5, e19568.

Mattsson, H.B., Balashova, A., Almqvist, B.S.G., Bosshard-Stadlin, S.A., Weidendorfer, D., 2018. Magnetic mineralogy and rock magnetic properties of silicate and carbonatite rocks from Oldoinyo Lengai volcano (Tanzania). J. Afr. Earth Sci. 142, 193–206.

McHenry, L.J., 2009. Element mobility during zeolitic and argillic alteration of volcanic ash in a closed-basin lacustrine environment: case study Olduvai Gorge, Tanzania. Chem. Geol. 265, 540–552.

McHenry, L.J., 2010. Element distribution between coexisting authigenic mineral phases in argillic and zeolitic altered tephra, Olduvai Gorge, Tanzania. Clay. Clay Miner. 58, 627–643.

McHenry, L.J., 2011. Geochemistry and mineralogy of Laetoli area tuffs: lower Laetolil through Naibadad beds. In: Harrison, T. (Ed.), Paleontology and Geology of Laetoli: Human Evolution in Context Volume 1: Geology, Geochronology, Paleoecology and Paleoenvironment. Springer, Dordrecht, pp. 121–141.

Mitchell, R.H., 2009. Peralkaline nephelinite–natrocarbonatite immiscibility and carbonatite assimilation at Oldoinyo Lengai, Tanzania. Contrib. Mineral. Petrol. 158, 589–598.

Mitchell, R.H., Dawson, J.B., 2012. Carbonate-silicate immiscibility and extremely per-alkaline silicate glasses from Nasira cone and recent eruptions at Oldoinyo Lengai Volcano, Tanzania. Lithos 152, 40–46.

Mollel, G.F., 2007. Petrochemistry and Geochronology of Ngorongoro Volcanic Highland Complex (NVHC) and its Relationship to Laetoli and Olduvai Gorge, Tanzania. PhD Thesis. Rutgers University, USA.

Mollel, G.F., Swisher III, C.C., 2012. The Ngorongoro volcanic highland and its relationships to volcanic deposits at Olduvai Gorge and east African rift volcanism. J. Hum. Evol. 63, 274–283.

Mollel, G.F., Swisher III, C.C., Feigenson, M.D., Carr, M.J., 2008. Geochemical evolution of Ngorongoro Caldera, Tanzania: implications for crust-magma interaction. Earth Planet. Sci. Lett. 271, 337–347.

Mollel, G.F., Swisher III, C.C., McHenry, L.J., Feigenson, M.D., Carr, M.J., 2009. Petrogenesis of basalt-trachyte lavas from Olmoti crater, Tanzania. J. Afr. Earth Sci. 54, 127–347.

Mollel, G.F., Swisher III, C.C., Feigenson, M.D., Carr, M.J., 2011. Petrology, geochemistry and age of Satiman, Lemagurut and Oldeani: sources of the volcanic deposits of the Laetoli area. In: Harrison, T. (Ed.), Paleontology and Geology of Laetoli: Human Evolution in Context Volume 1: Geology, Geochronology, Paleoecology and Paleoenvironment. Springer, Dordrecht, pp. 99–119.

Moore, D.N., Reynold, R.C., 1997. X-ray Diffraction and the Identification and Analysis of Clay Minerals. Oxford University Press, pp. 378.

Morizet, Ya, Iacono-Marziano, G., Kjarsgaard, B.A., 2013. Quantification of dissolved CO_2 in silicate glasses using micro-Raman spectroscopy. Am. Mineral. 98, 1788–1802.

Morizet, Ya, Paris, M., Gaillard, F., Scaillet, B., 2014. Carbon dioxide in silica-under-saturated melt. Part I: the effect of mixed alkalis (K and Na) on CO_2 solubility and speciation. Geochem. Cosmochem. Acta 141, 45–61.

Muirhead, J.D., Kattenhorn, S.A., Lee, H., Mana, S., Turrin, B.D., Fischer, T.P., Kianji, G., Dindi, E., Stamps, D.S., 2016. Evolution of upper crustal faulting assisted by magmatic volatile release during early-stage continental rift development in the East African Rift. Geosphere 12, 1670–1700.

Musiba, C.M., Mabula, A., Selvaggio, M., Magori, C.C., 2008. Pliocene animal trackways at Laetoli: research and conservation potential. Ichnos 15, 166–178.

Neukirchen, F., Finkenbein, T., Keller, J., 2010. The lava sequence of the east African Rift escarpment in the Oldoinyo Lengai – Lake Natron sector, Tanzania. J. Afr. Earth Sci. 58, 734–751.

Paslick, C., Halliday, A.N., James, D., Dawson, J.B., 1995. Enrichment of Continental lithosphere by OIB melts: isotopic evidence from the volcanic province of northern Tanzania. Earth Planet. Sci. Lett. 130, 109–126.

Paslick, C.R., Halliday, A.N., Lange, R.A., James, D., Dawson, J.B., 1996. Indirect crustal contamination: evidence from isotopic and chemical disequilibria in minerals from alkali basalts and nephelinites from northern Tanzania. Contrib. Mineral. Petrol. 125, 277–292.

Peters, C.R., Blumenschine, R.J., Hay, R.L., Livingstone, D.A., Marean, C.W., Harrison, T., Armour-Chelu, M., Andrews, P., Bernor, R.L., Bonnefille, R., Werdelin, L., 2008. Paleoecology of the Serengeti-Mara ecosystem. In: Sinclair, A.R.E., Packer, C., Mduma, S.A.R., Fryxell, J.M. (Eds.), Serengeti III. Human Impacts on Ecosystem Dynamics. The University of Chicago Press, Chicago and London, pp. 47–94.

Pickering, R., 1964. Endulen. Tanzania Geological Survey Quarter Degree Sheet 52.

Poppe, L.J., Paskevich, V.F., Hathaway, J.C., Blackwood, D.S., 2001. A Laboratory Manual for X-Ray Powder Diffraction. U. S. Geological Survey Open-File Report 01-041, pp. 88.

Reguir, E.P., Chakhmouradian, A.R., Halden, N.M., Yang, P., Zaitsev, A.N., 2008. Early magmatic and reaction-induced trends in magnetite from the carbonatites of Kerimasi, Tanzania. Can. Mineral. 46, 879–900.

Sekisova, V.S., Sharygin, V.V., Zaitsev, A.N., Strekopytov, S., 2015. Liquid immiscibility during crystallization of forsterite–phlogopite ijolites at Oldoinyo Lengai Volcano, Tanzania: study of melt inclusions. Russ. Geol. Geophys. 56, 1717–1737.

Sharygin, V.V., Kamenetsky, V.S., Zaitsev, A.N., Kamenetsky, M.B., 2012. Silicate-na-trocarbonatite carbonate liquid immiscibility in 1917 eruption combeite-wollastonite nephelinite, Oldoinyo Lengai volcano, Tanzania: melt inclusion study. Lithos 152, 23–39.

Simonetti, A., Bell, K., 1993. Isotopic disequilibrium in clinopyroxenes from nephelinitic lavas, Napak volcano, eastern Uganda. Geology 21, 243–246.

Strekopytov, S.V., Dubinin, A.V., 1997. Determination of Zr, Hf, Mo, W, and Th in standard reference samples of ocean sediments by inductively coupled plasma mass spectrometry. J. Anal. Chem. 52, 1171–1174.

Su, D.F., Harrison, T., 2015. The paleoecology of the upper Laetolil beds, Laetoli Tanzania: a review and synthesis. J. Afr. Earth Sci. 101, 405–419.

Sun, S., McDonough, W.F., 1989. Chemical and isotopic systematics of oceanic basalts: implications for mantle composition and processes. Spec. Publ. Geol. Soc. Lond. 42, 313–345.

Takahashi, Y., Tada, A., Shimizu, H., 2004. Distribution pattern of rare earth ions between water and montmorillonite and its relation to the sorbed species of the ions. Anal. Sci. 20, 1301–1306.

van der Watt, J.G., Waanders, F.B., 2012. Leaching of rare earth elements from bentonite clay. J. South. Afr. Inst. Min. Metall. 112, 281–285.

Wiedenmann, D., Zaitsev, A.N., Britvin, S.N., Krivovichev, S.V., Keller, J., 2009. Alumoåkermanite, $(Ca,Na)_2(Al,Mg,Fe^{2+})(Si_2O_7)$, a new mineral from the active carbonatite–nephelinite–phonolite volcano Oldoinyo Lengai, northern Tanzania. Mineral. Mag. 73, 373–384.

Wiedenmann, D., Keller, J., Zaitsev, A.N., 2010. Melilite-group minerals at Oldoinyo Lengai, Tanzania. Lithos 118, 112–118.

Wirth, K.R., Adelsberger, K.A., 2002. Mantle source and magmatic evolution of the late Pliocene Ogol lava beds of Laetoli, Tanzania. Geol. Soc. Am. Abstr. Progr. 34, 363.

Zaitsev, A.N., 2010. Nyerereite from calcite carbonatite of Kerimasi volcano, northern Tanzania. Geol. Ore Deposits 52 (7), 630–640.

Zaitsev, A.N., Chakhmouradian, A.R., 2002. Calcite-amphibole-clinopyroxene rock from the Afrikanda complex, Kola peninsula, Russia: mineralogy and a possible link to carbonatites. II Oxysalt minerals. Can. Mineral. 40, 103–120.

Zaitsev, A.N., Keller, J., Spratt, J., Jeffries, T.E., Sharygin, V.V., 2009. Chemical

composition of nyerereite and gregoryite from natrocarbonatites of Oldoinyo Lengai volcano, Tanzania. Geol. Ore Deposits 51, 608–616.

Zaitsev, A.N., Williams, C.T., Britvin, S.N., Kuznetsova, I.V., Spratt, J., Petrov, S.V., Keller, J., 2010. Kerimasite, $Ca_3Zr_2(Fe_2^{3+}Si)O_{12}$, a new garnet from carbonatites of Kerimasi volcano and surrounding explosion craters, northern Tanzania. Mineral. Mag. 74, 841–858.

Zaitsev, A.N., Wenzel, T., Spratt, J., Williams, T.C., Strekopytov, S., Sharygin, V.V., Petrov, S.V., Golovina, T.A., Zaitseva, E.O., Markl, G., 2011. Was Sadiman volcano a source for the Laetoli footprint tuff? J. Hum. Evol. 61, 121–124.

Zaitsev, A.N., Marks, M.A.W., Wenzel, T., Spratt, J., Sharygin, V.V., Strekopytov, S., Markl, G., 2012. Mineralogy, geochemistry and petrology of the phonolitic to nephelinitic Sadiman volcano, Crater Highlands, Tanzania. Lithos 152, 66–83.

Zaitsev, A.N., Wenzel, T., Vennemann, T., Markl, G., 2013. Tinderet volcano, Kenya – an old natrocarbonatite locality? Mineral. Mag. 77, 213–226.

Zaitsev, A.N., Spratt, J., Sharygin, V.V., Wenzel, T., Zaitseva, O.A., Markl, G., 2015. Mineralogy of the Laetolil footprint tuff: a comparison with possible volcanic sources from the Crater Highlands and Gregory rift. J. Afr. Earth Sci. 111, 214–221.

Zaitsev, A.N., Savchenok, A.N., Vlasov, D.Yu, Zelenskaya, M.S., 2016. Consultancy Services for Design, Construction & Supervision of Laetoli State of the Art Museum. Part I. Unpublished Report to Peter Rich Architects – GMP Consulting Engineers – Laetoli JV, St. Petersburg.

Zaitsev, A.N., Savchenok, A.N., Vlasov, D.Yu, Zelenskaya, M.S., 2017. Consultancy Services for Design, Construction & Supervision of Laetoli State of the Art Museum. Part II. Unpublished Report to Peter Rich Architects – GMP Consulting Engineers – Laetoli JV, St. Petersburg.